

1 Title:
2 The Shuram excursion: A response to climate
3 extremes at the dawn of animal life

4 Kristin D. Bergmann^{1*}, Magdalena R. Osburn², Julia Wilcots^{1,3},
Marjorie D. Cantine^{1,4}, Nicholas Boekelheide¹, Woodward W. Fischer⁵,
Magali Bonifacie⁶

¹Department of Earth, Atmospheric and Planetary Sciences,
Massachusetts Institute of Technology,
Cambridge, MA 02139

²Department of Earth and Planetary Sciences, Northwestern University
Evanston, IL 60208

³now at Department of Geosciences, Princeton University
Princeton, New Jersey

⁴now at Institut für Geowissenschaften, Goethe-Universität Frankfurt
Frankfurt, Germany

⁵Division of Geological and Planetary Sciences, California Institute of Technology
Pasadena, CA 91125

⁶Institut de Physique du Globe de Paris, Université Paris Cité
1 Rue Jussieu, 75005 Paris, France

*To whom correspondence should be addressed; E-mail: kdberg@mit.edu.

5 **The Ediacaran-aged Shuram excursion was the last and largest of the Neo-**
6 **proterozoic negative carbon isotope anomalies. Recognized in stratigraphic**
7 **successions around the globe, it precedes diverse evidence for macroscopic,**

8 multicellular life, and follows the Cryogenian global glaciations and Ediacaran
9 Gaskiers glaciation. Hypotheses for the cause of the Shuram excursion can be
10 broadly grouped into those that argue for post-depositional diagenetic alter-
11 ation of the carbon isotope record (1–7) and those that argue the extremely low
12 $\delta^{13}\text{C}$ values reflect a primary perturbation to the carbon cycle (8–10). Given
13 the timing and magnitude of this event, evaluating these disparate hypotheses
14 is critical for reconstructing the environmental conditions under which com-
15 plex life evolved on Earth. We test specific predictions of each model using
16 a range of stratigraphic observations and micro- and macro-analytical tech-
17 niques. We find that the type sections in Oman where the Shuram excursion
18 was first described are well-preserved and contain a range of features difficult
19 to reconcile with a post-depositional origin. Many salient features of these sec-
20 tions, however, can be well-explained by an extreme warming event coupled
21 to a carbon cycle perturbation, analogous to the Paleocene-Eocene Thermal
22 Maximum (PETM), and increased middle Ediacaran volcanism. We propose
23 that both mass extinction and the diversification of Ediacaran eukaryotes, in-
24 cluding animals, were driven by temperature changes across the Shuram ex-
25 cursion.

26 One sentence summary: Macro- and micro-scale sedimentological and geochemical obser-
27 vations of Earth’s largest negative carbon excursion support its interpretation as an extreme
28 hyperthermal event.

29 **Main Text:** Neoproterozoic sedimentary successions record a series of pronounced negative
30 carbon isotope excursions. The most extreme of these, the Ediacaran-aged Shuram carbon
31 isotope excursion (CIE), drops from baseline $\delta^{13}\text{C}_{VPDB}$ values of +5‰ to as low as 12‰ within

32 tens of meters of vertical stratigraphic section, and then gradually recovers to +5‰ often over
33 several hundred meters, in multiple sections globally (11). The Shuram excursion has been
34 hypothesized to result either from secondary (diagenetic) processes that postdate deposition
35 (1–7) or from primary changes in water column dissolved inorganic carbon (DIC) (8, 9, 12).

36 Arguments for a diagenetic origin for the Shuram excursion include: the extreme magnitude
37 of negative values in the nadir, beyond mantle input values which challenge traditional global
38 carbon isotope budget models (1, 13); high Mn/Sr and Fe/Ca ratios in the excursion nadir (3);
39 and the association of low $\delta^{13}\text{C}$ values with anomalously low $\delta^{18}\text{O}$ values—geochemical fea-
40 tures often interpreted as signatures of carbonate diagenesis (2, 3, 11). It has been suggested that
41 diagenesis could have produced the Shuram excursion either by flushing large volumes of ^{13}C -
42 poor fluids through carbonate rocks (fluid-buffered alteration) either early or late in the burial
43 history (2, 3, 6) or by the authigenic precipitation of cements and other secondary carbonates
44 from pore fluids with low $\delta^{13}\text{C}$ values driven by microbial processes associated with organic
45 diagenesis (sediment-buffered alteration) (1, 7, 14). Additional models based on Ca isotopic pat-
46 terns suggest that some stratigraphic intervals of the stratigraphy experienced sediment-buffered
47 alteration while others experienced fluid-buffered alteration (4, 5, 15). Each diagenetic model
48 makes specific predictions for the characteristics of rocks recording the excursion, including the
49 petrographic phases present; their geochemical variability at small spatial scales; the tempera-
50 tures they record in carbonate clumped isotopes; and the composition of the fluid from which
51 they precipitated (16)(Table 1).

52 A primary origin for the Shuram excursion is supported by the wide paleogeographic occur-
53 rence of middle Ediacaran negative CIEs. Concurrent Re/Os ages from the CIEs in Oman and
54 NW Canada also suggest the Shuram excursion is a primary carbon cycle perturbation with a
55 shorter duration than previously suggested (17). Five locations (Oman, NW Canada, Australia,

56 Peru, and Southern California) have similar isotopic (C, O, Ca, Sr) and bulk elemental patterns
57 (Mn, Sr, Mg) (15). When viewed as a whole, the geochemical data preserve clear trends as-
58 sociated with a primary depositional depth gradient (15). Stratigraphy in Australia preserve
59 depleted clasts in breccias deposited soon after the excursion nadir (18). High resolution $\delta^{13}\text{C}$
60 trends preserve evidence of a landward transgression of an ooid grainstone in Southern Cali-
61 fornia (19). Five other locations also demonstrate a clear association between the onset of the
62 excursion and sea level rise (15, 20). These locations have other sedimentological features in
63 common including climbing wave ripples and storm deposits including edgewise conglomer-
64 ates (15, 21–23).

65 In the Phanerozoic, there is a widely recognized relationship between climate change and
66 many CIEs identified globally (24–26), in part expressed as co-variation in $\delta^{13}\text{C}$ and $\delta^{18}\text{O}$, a
67 key feature of the Shuram Excursion. Coupled climate and carbon cycle perturbations like the
68 Paleocene-Eocene thermal maximum (PETM) are recorded in a wide range of sedimentologic
69 and isotopic datasets. During the PETM, a CO_2 or methane-driven temperature increase is
70 recorded by multiple proxies including Mg/Ca ratios of foraminifera and carbonate clumped-
71 isotope temperature change in marine and terrestrial environments (27, 28). Physical conse-
72 quences of warming include the thermal expansion of seawater and subsequent sea level rise,
73 as well as a flashy hydrologic cycle characterized by severe and frequent storms (29, 30). Many
74 deep-sea cores show a characteristic red clay interval associated with the PETM event horizon
75 in otherwise carbonate-rich strata which has been interpreted as a sedimentological expression
76 of carbonate dissolution following ocean acidification and a shoaling of the carbonate com-
77 pensation depth (CCD) (31). Shallow water environments document a smaller magnitude pH
78 change. Both deep and shallow oceans contribute CO_2 release to the atmosphere (32). Anoxia
79 and expanded oxygen minimum zones, in part due to temperature-dependent O_2 solubility, can

80 be tracked with a variety of proxies including biomarkers and I/Ca (33, 34). An initial period of
81 rapid physical weathering in a hot and arid climate with minimal chemical breakdown is repre-
82 sented by sands and micaceous silts at multiple localities (35). A transition to a warm and wet
83 climate led to significant chemical weathering and deposition of kaolinites (36) and geochem-
84 ical proxy evidence for enhanced weathering (i.e. $^{187}\text{Os}/^{188}\text{Os}$) (37). Biologic consequences
85 from warming, anoxia, and ocean acidification include extinction, migration and origination in
86 both terrestrial and marine fossil records (38).

87 Different hypotheses for the driving mechanism of the Shuram excursion make distinct pre-
88 dictions that can be evaluated using the rock record (Table 1). We evaluate predictions from
89 each diagenetic model using sedimentology and stratigraphy, petrography, mineralogy, a range
90 of micro-and macro-analyses of trace element and isotopic variability, and carbonate clumped
91 isotope thermometry. We compare these results with observations of the PETM, a Phanerozoic
92 hyperthermal, to argue that the Shuram represents a similar, though more extreme, event. We
93 also compile known volcanic occurrences within the age range of the Shuram excursion (17)
94 and identify a potential driver for climate change. If a primary coupled climate-carbon cycle
95 perturbation model unifies the range of observations associated with Shuram excursion-hosting
96 strata worldwide, the magnitude of $\delta^{18}\text{O}$ change predicts this is one of the most extreme surface
97 ocean warming events in the last 600 million years.

98 **Results and Discussion** To test predictions from post-depositional diagenetic and primary
99 models for the Shuram excursion, two stratigraphic sections were studied from shallowly buried
100 strata in the Huqf outcrop area (Mukhaibah Dome (MD) & Khufai Dome (KD), < 2 km max
101 burial depth) (16, 39). The two sites preserve a range of shallow marine depositional environ-
102 ments through time.

103 **Sedimentology and Stratigraphy** Detailed lithofacies and sequence stratigraphic analysis
104 allows us to assess the sedimentological and stratigraphic predictions of each proposed mech-
105 anism against the rock record (Table 1). The Shuram excursion in Oman is recorded in the
106 strata of the Khufai, Shuram and Buah formations within the Ediacaran- to Cambrian-aged
107 Huqf Supergroup (20, 40, 41)(Fig. S1). In the Huqf Outcrop Area, the pre-excursion strata
108 of the Khufai Formation transition from deep-water calcitic mudstone and wackstone lithofa-
109 cies to shallow water dolomitic tepees, stromatolites, and edgewise conglomerates consistent
110 with a peritidal and shallow subtidal depositional environment (20)(Fig. 1A,E). The onset of
111 the Shuram excursion coincides with sea level rise recorded in a transgressive dolomitic oolite,
112 stromatolite, and mudstone lithofacies of the uppermost Khufai Formation ($\delta^{13}\text{C}_{VPDB}$ of 1 to
113 5.3‰)(Fig. 1B,F) (20, 42). The nadir of the excursion ($\delta^{13}\text{C}_{VPDB}$ of 8 to 12‰) is recorded in
114 subtidal, cross-stratified, calcitic ooid grainstones and edgewise conglomerates, that are inter-
115 calated with hummocky cross-stratified, red, micaceous, siliciclastic siltstones in the Shuram
116 Formation (41)(Fig. 1C,G). The recovery of the excursion ($\delta^{13}\text{C}_{VPDB}$ values of 8 to $+2\text{‰}$)
117 occurs in a thick limestone succession (~ 200 m) of subtidal crinkly laminated mudstone, edge-
118 wise conglomerates and large meter-scale domal stromatolites of the Buah Formation (43)(Fig.
119 1D,H). A sequence boundary occurs near the contact between the Shuram Formation and Buah
120 Formation as evidenced by increased sand, lenticular to wavy lamination, and evaporite mineral
121 laths. As a whole, the lithofacies in the nadir and recovery of the Shuram excursion suggest
122 storm-dominated conditions (Fig. 1). Climbing ripples and loading structures including
123 ball and pillow structures from dewatering indicate rapid sedimentation during the nadir.

124 **Petrography** To evaluate the predictions from sediment- and fluid-buffered diagenesis in car-
125 bonate microfacies (Table 1), we examined petrographic thin sections from throughout the ex-
126 cursion. Well below the onset of the excursion, the lower Khufai Formation has coarsely crys-

127 talline fabrics, evidence of dissolution and veining in the calcitic deep water mudstones and
128 wackstones (Fig. 2F, Fig. S1). However, the carbonates from just below, in the Shuram excur-
129 sion, and after it preserve small crystal sizes of micrite and microspar in mudstones, and ooids
130 with optically oriented, radial crystal fabrics (16, 20, 44)(Fig. 2A-E).

131 Ooids—spherical carbonate grains that form in shallow water environments—are particularly
132 useful in evaluating alteration processes because these grains precipitate directly from seawater
133 and, if primary fabrics are preserved, distinct crystal patterns are observable. There are
134 two separate oolitic intervals capturing the Shuram excursion. One bed, 5–20 m thick, at the
135 top Khufai Formation captures the onset of the excursion ($\delta^{13}\text{C}_{VPDB}$ values of 0 to 5‰)(Fig.
136 1B,F,2B). This bed also includes mudstone rip-up clasts and micritic stromatolites that nucle-
137 ated on the grainstone and generated synoptic topography above the oolite(Fig. 1C). The second
138 oolitic interval is in the nadir of the excursion ($\delta^{13}\text{C}_{VPDB}$ values of 9 to 12‰). Oolite beds are
139 interbedded with siltstones spanning a 100 m interval in the Shuram Formation(Fig. 1C,2D,E).

140 We utilized petrography, EBSD, and SEM to quantify crystal sizes and orientations of ooid
141 fabrics from the onset and nadir of the excursion. The dolomite ooids from the onset of the
142 excursion preserve a radial, plumose fabric composed of fine crystals as seen in nano-scale
143 synchrotron-based PIC mapping and EBSD (16, 20, 44)(Fig. 3A,B). The ooids are often silica-
144 cemented or silicified, particularly in the northern Huqf outcrop area (16, 20, 44)(Fig. 2B). In
145 SEM after cryo-fracturing, there is also significant authigenic Mg silicate clay present, likely
146 palygorskite because of its minor Al and microfibrillar fabric (Fig. 3E,F). The dolomite crystals
147 often appear to template on the palygorskite on the outer rind of the nucleus and in the cortex,
148 replicating the curved shapes and interlocking, fibrous matted textures (Fig. 3C,F).

149 The calcitic ooid grainstones from the nadir of the excursion ($\delta^{13}\text{C}_{VPDB}$ values of -8 to
150 -12‰) in the Shuram Formation are often trough cross-stratified, and in thin section contain
151 alternating siliciclastic and cement-rich horizons that infill around the ooids (Fig. 1C, 2D,E).
152 These ooids also have a radial fabric and are composed of elongate crystals that do not display
153 micritization or equant-mosaic replacement texture. Electron backscatter diffraction (EBSD)
154 demonstrates the radial crystals within the calcite ooids are oriented with the c-axis parallel to
155 growth direction (Fig. 3G,H,I). Pore-filling cements can inherit the orientation of the nearest
156 ooid crystal, but in general are blocky and randomly oriented. The radial calcite crystals are
157 larger, more planar, and always length-fast compare to the dolomite crystals in Fig. 3A and B.

158 **Mineralogy** To better characterize the mineralogy of the carbonates hosting the Shuram ex-
159 cursion, and to determine whether variability represents selective alteration of primary arago-
160 nite (4), or some other process, we used XRD, electron backscatter detection (EBSD), electron
161 microprobe elemental mapping and spot analysis, and strong- and weak-acid bulk-dissolutions
162 using inductively coupled atomic emission spectrometry.

163 The dolomite facies of the Upper Khufai Formation are ordered, stoichiometric dolomite
164 today, including the transgressive oolite described above with co-associated Mg silicate clays
165 and silica cements. Together the crystal structure and mineral co-associations provide good
166 evidence these dolomite ooids formed as primary dolomite (44). Combined this could suggest
167 alkaline conditions with high activities of Si and Mg, which may have aided in primary dolomite
168 formation (45).

169 A stratigraphically coherent mineralogical change from dolomite to limestone at the bound-
170 ary with the Shuram Formation is confirmed with both x-ray diffraction (XRD) and bulk trace
171 metal data. Electron microprobe spot analyses of individual calcitic ooids in the nadir of the

172 Shuram excursion indicate low Mg and Sr concentrations (Mg: mean $0.44 \pm 0.01\%$, Sr: 124
173 ± 29 ppm, Fe: 1712 ± 133 ppm, Mn: 815 ± 48 ppm, ± 1 S.E.)(Table S1), and, along with the
174 radial ooid fabric observed in Fig. 3G,H,I, further support a primary calcite mineralogy for this
175 interval.

176 In contrast, EPMA spot analyses in the stratigraphy that records the recovery from the Shuram
177 excursion can have Sr concentrations as high as $1596 \text{ ppm} \pm 29 \text{ ppm}$, indicating this interval
178 might have been primary aragonite prior to dissolution and calcite replacement. Despite this
179 process, the mudstones, edgewise conglomerates, and crinkly laminites are still micrite and
180 microspar, thus the transformation likely occurred under sediment-buffered conditions.

181 The macro-scale observations of mineralogical changes are common across many Shuram
182 excursion-bearing successions (15, 19). Our results, while surprising, suggest this is best un-
183 derstood as changing conditions in shallow marine environments to promote primary dolomite
184 precipitation in the excursion onset, primary calcite precipitation in the nadir, and finally pri-
185 mary aragonite precipitation in the recovery.

186 **Trace elements** Some hypotheses suggest that high concentrations of Fe and Mn measured
187 from bulk dissolution of rocks from the nadir of the excursion reflect the addition of Fe^{+2} and
188 Mn^{+2} from reduced fluids during diagenesis (1, 3)(Fig. S2). We tested these hypotheses us-
189 ing three methods: 1. electron microprobe (EPMA) elemental mapping and spot analysis, 2.
190 comparisons between analyses of strong- and weak-acid bulk-dissolutions using inductively
191 coupled atomic emission spectrometry, and 3. synchrotron x-ray absorption near-edge spec-
192 troscopy (XANES).

193 EPMA maps of Fe and Mn show spatial variability, not homogeneously distributed elemen-
194 tal enrichment associated with dissolution and reprecipitation in low oxygen pore fluids (Fig.
195 4). High iron concentration in EPMA spot analyses within ooids can be attributed to ultrafine
196 inclusions of hematite, likely detrital in origin ($<1 \mu\text{m}$)(Fig. 4I, Fig. S5, S6). Some authigenic
197 hematite coating detrital grains and mineralized ooids along surfaces likely represents miner-
198 alization during depositional hiatuses(Fig. 4I, Fig. S5). These surfaces are often capped by
199 intervals lean in detrital sediments but rich in secondary cement, indicating faster ooid deposi-
200 tion. XANES analyses indicate that iron is present primarily as Fe(III) in hematite and mixed
201 valence in biotite (Fig. S4).

202 The high bulk Mn contents of the oolitic grainstones (up to 3670 ppm) exceeds those of the
203 individual ooids (mean 815 ± 48 ppm, ± 1 S.E.) and can be attributed to manganese-rich pink
204 cements (Mg: mean $0.37 \pm 0.02\%$, Sr: 0 ppm, Fe: 647 ± 165 ppm, Mn: 7853 ± 587 ppm, ± 1
205 S.E.), which fill interstices between ooids (Fig. 4O, Fig. S6). These pink cements constitute a
206 diagenetic fabric, and confirm that the high Mn contents of Shuram rocks are a result of post-
207 depositional processes. However, these pink cements pre-date a second, porosity-occluding,
208 sparry calcite cement (Mg: mean $0.33 \pm 0.02\%$, Sr: 141 ± 37 ppm, Fe: 912 ± 109 ppm,
209 Mn: 1532 ± 106 ppm, ± 1 S.E.) indicating they formed during early diagenesis in the shallow
210 sediments (Fig. 2D, Fig. 4, Fig. S6). XANES analysis indicates that most of the manganese
211 is divalent Mn(II) and contained in manganoan calcite (Fig. S4). Iron oxides also host smaller
212 amounts of manganese (visible in both EDS and electron microprobe maps; Fig. 4J).

213 Thus high bulk iron concentrations, previously inferred to represent carbonate dissolution
214 and reprecipitation in low oxygen burial fluids, are better explained as artifacts of leaching
215 procedures using strong acids which dissolve detrital hematite and minor authigenic hematite,
216 associated with silts. In contrast, Mn enrichments reflect diagenetic addition of Mn^{+2} in the

217 earliest stages of sedimentation and cementation, presumably during or immediately after ooid
218 deposition. In support of very early Mn cycling, we also observe Mn-rich banding within the
219 dolomite ooids associated with the onset of the Shuram excursion at the top of the Khufai
220 Formation (44)(Fig. 4E).

221 **Phase-specific isotopic heterogeneity** Some models suggest the Shuram excursion can be
222 explained by the presence of isotopically light, secondary authigenic carbonate cements (1,
223 7, 14). We used Secondary Ion Mass Spectrometry (SIMS) to analyze disparate carbonate
224 phases formed at different times (ooids, early Mn-rich pink cements, and clear blocky porosity-
225 occluding cement). Authigenic explanations for the low $\delta^{13}\text{C}$ values characteristic of the Shu-
226 ram excursion would predict the Mn-rich and/or porosity occluding blocky cements would have
227 lower ^{13}C values relative to the ooids. This is not observed; in contrast, SIMS analysis of two
228 samples from a similar stratigraphic horizon, but located ~ 15 km apart, shows that ooids have
229 similar carbon and oxygen isotopic compositions to both authigenic early manganese-rich pink
230 cements, and porosity-occluding blocky spar cements (Fig. 4F,K, Fig. S6). The relatively
231 homogeneous measurements of ooids and cements suggests that these phases reflect primary
232 conditions and precipitated from similar fluids and temperatures or were pervasively altered
233 by fluid-buffered diagenesis. Within the context of the above petrographic and trace element
234 variability of these three phases, the former is more likely.

235 **Crystallization temperature and fluid composition** To further evaluate predictions of fluid-
236 and sediment-buffered diagenesis at various points in the stratigraphy, carbonate clumped iso-
237 tope thermometry analyses were performed on a range of carbonate facies. Carbonates with
238 different initial characteristics (e.g., porosity, permeability, and mineralogy) will experience
239 variable fluid-sediment interaction, which can result in co-variation of the fluid/sediment reac-
240 tion temperature, carbonate $\delta^{18}\text{O}_{VPDB}$, and water $\delta^{18}\text{O}_{VSMOW}$. Cross-plots of these variables

241 will differentiate between packages of rocks that underwent fluid- or sediment-buffered alter-
242 ation. If any of the intervals (including the transgressive dolomites (0 to -5‰) or the calcites of
243 the nadir (~ -7 to -12‰) capturing parts of the Shuram excursion experienced fluid-buffered
244 alteration in the Huqf as suggested in previous studies (1, 3, 4, 15), a diverse suite of samples
245 should reveal a trend of increasing reaction temperature at relatively invariant $\delta^{18}\text{O}_{VSMOW}$ of
246 water—near 0‰ if fluids are marine or more ^{18}O -depleted water if meteoric. If, instead, lithifi-
247 cation or alteration occurred in sediment-buffered conditions, then water $\delta^{18}\text{O}$ and temperature
248 will increase while carbonate $\delta^{18}\text{O}$ remains constant.

249 When plotted in this space, carbonates from the lower Khufai have the highest temperatures,
250 are macroscopically coarsely crystalline, and are associated with petrographic observations in-
251 dicating fluid flow including veining (Fig. 2F). Notably, $\delta^{13}\text{C}$ is not correlated with $\delta^{18}\text{O}$ in the
252 lower Khufai Formation, despite a more fluid-buffered diagenetic regime and this interval is
253 well below the onset of the Shuram excursion.

254 In contrast, the suite of pre-, onset-, and syn- Shuram-excursion carbonates analyzed from
255 the upper Khufai, Shuram and lower Buah formations have data trends indicating sediment-
256 buffered diagenesis (Fig. 2D). As a group, these carbonates show exceptional textural preserva-
257 tion, moderate clumped isotope temperatures ($38\text{--}78^\circ\text{C}$) and precipitation from fluids with oxy-
258 gen isotope compositions similar to the range observation across modern marine environments
259 ($\delta^{18}\text{O}_{VSMOW}$ of water = 2 to $+2\text{‰}$) (Fig. 2D). It is important to note that the temperature mea-
260 surements in Fig. 2 average the isotopic compositions of multiple carbonate phases—including
261 primary ooids and other grains, mud and diagenetic cements (i.e. they are bulk measurements
262 reflecting lithification). We note that mudstone, wackestone and finely laminated stromatolite
263 samples with small crystal sizes and evidence for early lithification like tepee structures and
264 carbonate intraclasts sit at the low-temperature end of the data trend in Fig. 2 (i.e. Fig. 2C,

265 Table S1) (16). Petrographic analysis of higher temperature samples indicate they are more
266 heterogeneous, richer in secondary cements, and occur occasionally throughout the excursion
267 (Fig. 2B,E,F) (16). The nadir carbonate in particular suggest sediment-buffered conditions (i.e.
268 near constant $\delta^{18}\text{O}$).

269 **Diagenetic alteration of strata hosting the Shuram excursion** While diagenesis has cer-
270 tainly played a role in the observed rock record in Oman, we argue based on the above observa-
271 tions that the Shuram excursion as expressed in Oman departs from the diagenetic expectations
272 of post-depositional Shuram excursion models (Table 1). Models for a diagenetic origin for
273 the Shuram excursion call on a range of post-depositional processes. Models that suggest the
274 Shuram excursion is the result of fluid-buffered diagenesis by either meteoric (2, 6) or basinal
275 fluids (3) predict fabric destruction, trace element homogeneity, and coarsening of crystal size
276 (Table 1). Yet in the Huqf region of Oman, carbonates hosting the Shuram excursion are notable
277 for their well-preserved fabrics, fine crystal sizes, and spatially-distinct trace element distribu-
278 tions (Figs. 2, 3, 4). Multiple fluid-buffered diagenetic models also predict low meteoric or high
279 basinal fluid $\delta^{18}\text{O}_{VSMOW}$ values to explain the large negative $\delta^{18}\text{O}$ excursion (2, 3). These dis-
280 tinct oxygen isotope compositions are inconsistent with seawater-like fluid $\delta^{18}\text{O}_{VSMOW}$ values
281 calculated from mineral $\delta^{18}\text{O}$ and Δ_{47} -temperature measurements of these strata (Fig. 4).

282 Models suggesting that the Shuram excursion is the result of syn-sedimentary remineral-
283 ization of organic matter resulting in extremely light authigenic carbonates predict a signifi-
284 cant difference in $\delta^{13}\text{C}$ between authigenic cements and primary carbonates (1, 7, 14)(Table 1).
285 There is an early authigenic phase in shallow marine environments in Oman—pink Mn-rich
286 cements—that partially cements ooids. However, our geochemical measurements document
287 minimal isotopic heterogeneity across the multiple carbonate phases preserving the nadir (Fig.
288 3, Fig. S6). This isotopic homogeneity exists despite preserved elemental heterogeneity and

289 crystallographic differences between each phase, suggesting the isotopically light carbonates
290 reflect precipitation from DIC rather than wholesale dissolution and reprecipitation (Fig. 3).
291 Results are consistent with those from calcitic micrites in Australia (46). The only phase in
292 those rocks with a distinct carbon isotopic composition are isotopically heavy dolomite rhombs
293 of uncertain timing (46).

294 Another model has suggested that all carbonate sediments of this interval began as aragonite
295 with light Ca isotopic compositions and high Sr concentrations, using the modern Bahamian
296 platform as an analog, and some intervals underwent selective fluid-buffered alteration to pro-
297 duce heavy Ca isotopic intervals with low Sr concentrations (4, 15, 47)(Table 1). This model
298 predicts that Oman, out of all the locations globally that preserve the Shuram excursion, hosts
299 the most diagenetically altered strata because it has the highest Ca isotopic values (15). The in-
300 terval with the heaviest Ca isotopic values, the dolomitic ooids capturing the onset of the excu-
301 sion, would have experienced significant fluid flushing during a transformation from aragonite
302 to dolomite. Instead, the above petrographic, geochemical, and isotopic observations suggest
303 that three changes in the primary depositional mineralogy are a key component of the excursion
304 (also see the Ocean Acidification and Recovery section below).

305 **Evidence for a coupled climate-carbon cycle event** Diagenetic alteration cannot account
306 for our multi-proxy observations of the carbonates hosting the Shuram excursion in Oman. We
307 instead explore our results in the context of the predictions of a coupled climate-carbon cycle
308 model (Table 1) using the rich marine and terrestrial records of the PETM. We identify six
309 predictions for a climate-carbon cycle perturbation, which have ramifications for the oceans,
310 atmosphere, land, and biosphere. Alongside co-varying $\delta^{13}\text{C}$ and $\delta^{18}\text{O}$ isotopic records, these
311 predictions are: [1] warming with an identifiable driver, [2] sea level rise and storms, [3] en-
312 hanced physical and chemical weathering, [4] ocean acidification, [5] anoxia, and [6] extinction

313 and radiation.

314 **[1] Warming with Driver:** To consider whether the Shuram excursion coincides with vol-
315 canic activity capable of driving a climate event, we built an inclusive database of Neoprotero-
316 zoic occurrences of intrusive and extrusive igneous rocks. We classified each unit with com-
317 positional information and age constraints. The time interval of the Shuram excursion (574.0
318 ± 4.7 to 567.3 ± 3.0 Ma) (17), coincides with a peak in occurrences of volcanic rocks,
319 specifically, carbonatites (Fig. 5H). These CO₂-rich volcanic rocks are particularly abundant
320 relative to other time intervals of the Neoproterozoic. Large, caldera-style carbonatite deposits
321 can be found associated with the Central Iapetus Magmatic Province (48), including the Alnö
322 complexes in Scandinavia (49, 50), the Vesely and Pogranichnoe complexes in Russia (51), the
323 Sarfartoq complex in West Greenland (52), and those associated with the Pan-African orogeny
324 in Africa (53–56) and Argentina (57). Carbonatite-derived zircons contribute to a significant
325 peak at 576 Ma in detrital zircon spectra from Antarctica (58).

326 Our high resolution clumped-isotope thermometry (Δ_{47}) dataset from the Huqf area of Oman
327 documents cooler temperatures in the pre-excursion and recovery strata compared with higher
328 temperatures associated with the onset and nadir of the excursion (Fig. 2, Fig. S7). Interpreted
329 within the context of a 600-million-year Δ_{47} record from Oman (16), solid state reordering is
330 likely insignificant in the Huqf region (42). While we interpret the measured Δ_{47} -temperatures
331 of these bulk rocks as somewhat elevated from depositional temperatures because they are com-
332 posed of mixtures of primary sediments and shallow burial cements, the similarity of SIMS $\delta^{18}\text{O}$
333 data of ooids and cements suggests that the coldest clumped isotope temperatures in each time
334 bin approach primary temperatures in this coastal, shallow marine, tropical environment. The
335 broad change in temperature across the excursion may be significant because it is preserved in a
336 range of lithofacies (both dolomites and calcites) with a range of primary porosities. Based on

337 these results we propose that the largest negative $\delta^{13}\text{C}$ excursion on record was coincident with
338 an increase in shallow, coastal marine temperatures, perhaps as large as $\sim 12^\circ\text{C}$ followed by a
339 cooling of $\sim 15^\circ\text{C}$ (Fig. 4). Compiling the $\delta^{18}\text{O}$ of Ediacaran rock successions and accounting
340 for mineralogy, many successions suggest warming followed by cooling of similar magnitudes
341 assuming seawater $\delta^{18}\text{O}$ of -1.2‰ (Fig. 5G, Fig. S8, Fig. S9). The carbonate $\delta^{18}\text{O}$ compositions
342 in some sections are more clearly affected by deep burial alteration, however the broad pattern
343 of concurrent $\delta^{13}\text{C}$ and $\delta^{18}\text{O}$ change is preserved (i.e. Death Valley region, Fig. S8, Fig. S9).

344 While we recognize that this temperature change is large, multiple aspects of the Ediacaran
345 system may have contributed to its large magnitude relative to many Phanerozoic hyperther-
346 mals. Exact amounts of CO_2 from Ediacaran volcanic provinces are unknown, but carbon-
347 atites can have more CO_2 than mafic volcanics. There is also evidence for methane associated
348 with Shuram excursion strata (14), which, if significant, could amplify rapid climate warm-
349 ing. Additionally, the DIC reservoir in the Ediacaran may have been larger (59, 60) than in the
350 Cenozoic (32). Intriguingly, where the Shuram excursion is associated with carbonatites and
351 warming, the Gaskiers glaciation and cooling, is associated with an increase mafic volcanic
352 rocks (Fig. 5).

353 **[2] Sea level rise and storms:** Both sedimentological and geochemical evidence from Oman
354 suggest sea level rise at the onset of the Shuram excursion. Facies associated with subaerial
355 exposure, evaporation, and basinal restriction, including tepees, fenestral mudstones, intraclast
356 conglomerates, and small, laterally linked, stromatolites, are capped by facies that record trans-
357 gression during the onset of the excursion (Fig. 1, Fig. 5E) (20). Sedimentological features
358 documenting sea level rise at the onset of the excursion are consistent features across many
359 sections globally (15, 19). Sea level rise could be caused by thermal expansion of seawater from
360 warming, melting of high latitude glaciers, or displacement from young, buoyant oceanic crust

361 associated with the opening of the Iapetus Ocean.

362 Facies present in the excursion nadir and recovery host storm deposits including hummocky
363 cross-stratified silts, climbing wave ripples in deeper water environments and edgewise con-
364 glomerates across broad areas of Oman, Death Valley, NW Canada, and Australia (Fig. 1, Fig.
365 5E) (15, 21, 22). Strata containing these features are stacked for hundreds of vertical meters. A
366 transition in the hydrologic cycle to more stormy conditions is consistent with warming, and is
367 observed during the PETM (30, 61).

368 **[3] Weathering:** Grain-scale observations of the voluminous silts associated with the Shuram
369 excursion nadir in Oman and Death Valley, including grain size and mineralogy, may be consis-
370 tent with wind-blown loess filling accommodation in shallow water environments (62, 63)(Fig.
371 5E). A significant volume of detrital hematite is present in both locations (Fig. S5) (63),
372 which we suggest is analogous to climate-driven detrital hematite enrichments within PETM
373 deposits (64). Poorly weathered biotites, that are abundant within the siltstones associated with
374 the nadir of the excursion (Fig. 4, Fig. S5) gradually disappear in the recovery, which we link to
375 a switch from hot and dry conditions in the nadir of the excursion to warm and wet conditions
376 in the recovery, again analogous to PETM deposits (35–37, 65). The Sr isotope record also indi-
377 cates more radiogenic values consistent with chemical weathering (66)(Fig. 5D). The physical
378 and geochemical observations of sediments deposited during the Shuram excursion are con-
379 sistent with a concurrent land-based weathering and hydrologic cycle feedback that promoted
380 global cooling through silicate weathering (67).

381 **[4] Ocean Acidification and Recovery:** We document textural, chemical, and isotopic evi-
382 dence for primary mineralogical transformations associated with the Shuram excursion consis-
383 tent with CO₂-driven ocean acidification and recovery. The onset of the excursion is captured

384 in a grainstone of radial, plumose dolomite ooids with small crystal sizes ($\delta^{13}\text{C}_{VPDB} = +2$ to
385 6‰) (44) and micritic stromatolite bioherms (20). These are draped and overlain by poorly
386 consolidated siltstones, representing a carbonate gap perhaps linked to acidification. After 10s
387 of meters, the appearance of radial to banded radial calcitic ooids intercalated with siltstones
388 with $\delta^{13}\text{C}_{VPDB}$ values of 10 to 12‰ may represent a shift from geochemical conditions disfa-
389 voring carbonate precipitation (44) to those favoring calcite precipitation (Fig. 3). Finally, the
390 limestones capturing the recovery of the Shuram excursion consistently record high Sr concen-
391 trations and light Ca isotopic compositions, consistent with a precursor aragonite mineralogy,
392 which requires a higher saturation state (15, 19, 21)(Fig. 5C). We interpret the mineralogical
393 changes as evidence of a pH drop and recovery following chemical weathering, as in more re-
394 cent ocean acidification events (31, 36). A smaller deep ocean carbonate reservoir (60, 68) may
395 help explain why evidence for significant ocean acidification and a subsequent recovery can be
396 found in such shallow environments. Consequences of acidification should be expected to vary
397 in severity both regionally and with water depth.

398 **[5] Anoxia:** A temperature increase of 10-17°C in shallow coastal environments, as described
399 above, would have implications for dissolved oxygen solubility. Early marine cements in the
400 nadir have elevated manganese concentrations, indicating low oxygen conditions in the shallow
401 sediments (Fig. 2, Fig. 4, Fig. S6). The early manganese-rich cement phase we have identified,
402 suggests that anoxic conditions were prevalent in the shallow sediments and perhaps transiently
403 in the water column. Yet the lack of pyrite implies sulfate reduction was less significant than
404 manganese and iron reduction. Expanded anoxia associated with climate perturbations may
405 amplify the importance of diagenetic processes (e.g. authigenic carbonate precipitation) and
406 prevalence of isotopically light carbonates from enhanced organic remineralization (24, 25) or
407 from methane clathrate destabilization (14).

408 Most sediments of the Shuram excursion are extremely organic lean, unlike modern anoxic
409 sediments. At higher temperatures, remineralization rates outpace carbon fixation rates and
410 net primary productivity declines (24, 25). Both processes may explain the paucity of organic-
411 rich black shales during the Shuram excursion, despite organic-rich intervals both prior to and
412 after the Shuram excursion in deep-water Oman successions (69). The isotopic composition of
413 preserved organic carbon is distinct in shallow and deep ocean records (70)(Fig. 5B). In Oman
414 and China, inner and outer shelf inorganic $\delta^{13}\text{C}$ and $\delta^{13}\text{C}_{org}$ records are negatively correlated,
415 whereas basinal records are positively correlated (9, 71, 72).

416 Spatial heterogeneity in elemental enrichments, organic abundance, and organic $\delta^{13}\text{C}$ dif-
417 ferences between shallow and deep-water environments in Oman are consistent with a high
418 temperature perturbation driving density and redox stratification in Ediacaran oceans. If car-
419 bonate deposition was initially sluggish and inhibited and the depositional area was largely
420 limited to shallow water environments (60, 68), the residence time of carbon could have been
421 longer, providing a mechanism to prolong the excursion.

422 **[6] Extinction and Radiation:** Coupled climate-carbon cycle perturbations have visible ef-
423 fects on the fossil record in the Phanerozoic, but extinctions are difficult to recognize in the
424 non-skeletal, largely microscopic, fossil record of the Neoproterozoic. That said, evidence
425 for extinction and subsequent origination is concurrent with the Shuram excursion. We es-
426 timate extinction and origination for microfossils, deep water Ediacaran fossils and shallow
427 water Ediacaran fossils based on individual occurrence data (42, 69, 73–77)(Fig. 5A). Many
428 ornamented, organic-walled acanthomorphic acritarch microfossils disappear from the paleon-
429 tological record at the onset of the Shuram excursion (77). Within the nadir of the excursion,
430 organic-walled acritarchs are simple and rare, while the recovery sees a diverse range of micro-
431 fossils (77, 78). Macrofossils of algae, soft-bodied Ediacaran fauna, and the first biomineraliz-

432 ing organisms, *Cloudina* and *Namacalathus*, also appear following the recovery (79), although
433 with new age constraints (69), many of the fauna appear in significantly younger strata (80).
434 This pattern of origination following a hyperthermal is also observed following the PETM and
435 other Phanerozoic warming events (38, 81). The appearance of large macroscopic Ediacaran
436 fauna first in deep water environments in Newfoundland and NW Canada and then in shallow
437 water environments globally (Fig. 5A), is parsimonious with an expectation that deep-water
438 environments remained cooler during and following a temperature perturbation (75, 82, 83).
439 The Shuram excursion may represent the best candidate documented thus far for a Precambrian
440 mass extinction, followed by a recovery period with innovation, origination, and niche expansion.
441 This suggests that the Shuram excursion represented a critical bottleneck and turning point
442 for the evolutionary advances required for macroscopic, multicellular animal life.

443 **Conclusions** In summary, our climate driven model with coupled carbon cycle effects unifies
444 a range of sedimentological, geochemical, and biological observations of the globally-
445 distributed Shuram excursion. Our investigation finds little evidence to support hypotheses
446 that interpret the Shuram excursion as a diagenetic event or artifact. Instead, sedimentological,
447 geochemical, and paleontological records provide evidence of sea level rise, increased storm
448 intensity, ocean acidification and anoxia, a concurrent terrestrial weathering event, and biotic
449 extinction and origination. Abundant carbonatite eruptions concurrent with the excursion provide
450 a potential driver. These observations pose challenges to our understanding of internal
451 feedbacks in the carbon cycle and climate system in deep time. We contend that the Shuram excursion,
452 the largest negative carbon isotope excursion in Earth History, is best understood as one
453 of the most extreme hyperthermal events yet documented, and as such was likely both a critical
454 bottleneck for complex life and also spurred origination of diverse soft-bodied Ediacaran fauna
455 in its aftermath.

References and Notes

1. D. P. Schrag, J. A. Higgins, F. A. Macdonald, D. T. Johnston, Authigenic carbonate and the history of the global carbon cycle. *Science* **339**, 540–3 (2013).
2. L. P. Knauth, M. J. Kennedy, The late Precambrian greening of the Earth. *Nature* **460**, 728–732 (2009).
3. L. A. Derry, A burial diagenesis origin for the Ediacaran Shuram-Wonoka carbon isotope anomaly. *Earth Planet. Sci. Lett.* **294**, 152–162 (2010).
4. J. A. Higgins, C. L. Blättler, E. A. Lundstrom, D. P. Santiago-Ramos, A. A. Akhtar, A.-S. Crü Ger Ahm, O. Bialik, C. Holmden, H. Bradbury, S. T. Murray, P. K. Swart, Mineralogy, early marine diagenesis, and the chemistry of shallow-water carbonate sediments. *Geochim. Cosmochim. Acta* **220**, 512–534 (2018).
5. A.-S. C. Ahm, C. J. Bjerrum, C. L. Blättler, P. K. Swart, J. A. Higgins, Quantifying early marine diagenesis in shallow-water carbonate sediments. *Geochim. Cosmochim. Acta* **236**, 140–159 (2018).
6. G.-Y. Wei, J. Wang, N. J. Planavsky, M. Zhao, E. W. Bolton, L. Jiang, D. Asael, W. Wei, H.-F. Ling, On the origin of Shuram carbon isotope excursion in South China and its implication for Ediacaran atmospheric oxygen levels. *Precambrian Research* **375**, 106673 (2022).
7. L. Jiang, N. Planavsky, M. Zhao, W. Liu, X. Wang, Authigenic origin for a massive negative carbon isotope excursion. *Geology* **47**, 115–118 (2019).
8. D. H. Rothman, J. M. Hayes, R. E. Summons, Dynamics of the Neoproterozoic carbon cycle. *Proc. Natl. Acad. Sci. USA* **100**, 8124–8129 (2003).

- 478 9. D. A. Fike, J. P. Grotzinger, L. M. Pratt, R. E. Summons, Oxidation of the Ediacaran
479 ocean. *Nature* **444**, 744–7 (2006).
- 480 10. C. J. Bjerrum, D. E. Canfield, Towards a quantitative understanding of the late Neopro-
481 terozoic carbon cycle. *Proc. Natl. Acad. Sci.* **108**, 5542–5547 (2011).
- 482 11. J. P. Grotzinger, D. A. Fike, W. W. Fischer, Enigmatic origin of the largest-known carbon
483 isotope excursion in Earth’s history (2011).
- 484 12. C. J. Bjerrum, D. E. Canfield, Towards a quantitative understanding of the late Neopro-
485 terozoic carbon cycle. *Proc. Natl. Acad. Sci.* **108**, 5542–5547 (2011).
- 486 13. T. F. Bristow, M. J. Kennedy, Carbon isotope excursions and the oxidant budget of the
487 Ediacaran atmosphere and ocean. *Geology* **36**, 863–866 (2008).
- 488 14. H. Cui, A. J. Kaufman, S. Xiao, C. Zhou, X.-M. Liu, Was the Ediacaran Shuram Excursion
489 a globally synchronized early diagenetic event? Insights from methane-derived authigenic
490 carbonates in the uppermost Doushantuo Formation, South China (2016).
- 491 15. J. F. Busch, E. B. Hodgin, A.-S. C. Ahm, J. M. Husson, F. A. Macdonald, K. D. Bergmann,
492 J. A. Higgins, J. V. Strauss, Global and local drivers of the Ediacaran Shuram carbon
493 isotope excursion. *Earth and Planetary Science Letters* **579**, 117368 (2022).
- 494 16. K. D. Bergmann, S. A. Al Balushi, T. J. MacKey, J. P. Grotzinger, J. M. Eiler, A 600-
495 million-year carbonate clumped-isotope record from the Sultanate of Oman. *J. Sediment.*
496 *Res.* **88**, 960–979 (2018).
- 497 17. A. D. Rooney, M. D. Cantine, K. D. Bergmann, I. Gómez-Pérez, B. Al Baloushi, T. H.
498 Boag, J. F. Busch, E. A. Sperling, J. V. Strauss, Calibrating the coevolution of Ediacaran
499 life and environment. *Proc. Natl. Acad. Sci. U. S. A.* **117**, 16824–16830 (2020).

- 500 18. J. M. Husson, A. C. Maloof, B. Schoene, A syn-depositional age for Earth's deepest $\delta^{13}\text{C}$
501 excursion required by isotope conglomerate tests. *Terra Nov.* **24**, 318–325 (2012).
- 502 19. K. Bergmann, R. Zentmyer, W. Fischer, The stratigraphic expression of a large negative
503 carbon isotope excursion from the ediacaran johnnie formation, death valley. *Precambrian*
504 *Res.* **188** (2011).
- 505 20. M. Osburn, J. Grotzinger, K. Bergmann, Facies, stratigraphy, and evolution of a middle
506 ediacaran carbonate ramp: Khufai formation, sultanate of Oman. *Am. Assoc. Pet. Geol.*
507 *Bull.* **98**, 1631–1667 (2014).
- 508 21. J. M. Husson, A. C. Maloof, B. Schoene, Stratigraphic expression of Earth's deepest $\delta^{13}\text{C}$
509 excursion in the Wonoka Formation of South Australia. *Am. J. Sci.* (2015).
- 510 22. E. Le Guerroué, P. A. Allen, A. Cozzi, Chemostratigraphic and sedimentological frame-
511 work of the largest negative carbon isotopic excursion in earth history: The neoproterozoic
512 Shuram formation (Nafun Group, Oman). *Precambrian Res.* **146**, 68–92 (2006).
- 513 23. E. Le Guerroué, P. A. Allen, A. Cozzi, Parasequence development in the Ediacaran Shu-
514 ram Formation (Nafun Group, Oman): High-resolution stratigraphic test for primary ori-
515 gin of negative carbon isotopic ratios. *Basin Res.* **18**, 205–219 (2006).
- 516 24. S. M. Stanley, Relation of Phanerozoic stable isotope excursions to climate, bacterial
517 metabolism, and major extinctions. *Proc. Natl. Acad. Sci. U. S. A.* **107**, 19185–19189
518 (2010).
- 519 25. S. Finnegan, D. A. Fike, D. Jones, W. W. Fischer, A Temperature-Dependent Positive
520 Feedback on the Magnitude of Carbon Isotope Excursions. *Geosci. Canada* **39** (2012).

- 521 26. S. K. Turner, Pliocene switch in orbital-scale carbon cycle/climate dynamics. *Paleo-*
522 *ceanography* **29**, 1256–1266 (2014).
- 523 27. D. Evans, N. Sahoo, W. Renema, L. J. Cotton, W. Müller, J. A. Todd, P. K. Saraswati,
524 P. Stassen, M. Ziegler, P. N. Pearson, *et al.*, Eocene greenhouse climate revealed by cou-
525 pled clumped isotope-Mg/Ca thermometry. *Proceedings of the National Academy of Sci-*
526 *ences* **115**, 1174–1179 (2018).
- 527 28. G. N. Inglis, M. J. Carmichael, A. Farnsworth, D. J. Lunt, R. D. Pancost, A long-term,
528 high-latitude record of Eocene hydrological change in the Greenland region. *Palaeogeogr.*
529 *Palaeoclimatol. Palaeoecol.* **537** (2020).
- 530 29. A. Sluijs, U. Röhl, S. Schouten, H. J. Brumsack, F. Sangiorgi, J. S. Sinninghe Damsté,
531 H. Brinkhuis, late Paleocene - Early Eocene paleoenvironments with special emphasis on
532 the Paleocene-Eocene thermal maximum (Lomonosov Ridge, Integrated Ocean Drilling
533 Program Expedition 302). *Paleoceanography* **23**, PA1S11 (2008).
- 534 30. M. J. Carmichael, R. D. Pancost, D. J. Lunt, Changes in the occurrence of extreme precip-
535 itation events at the Paleocene–Eocene thermal maximum. *Earth and Planetary Science*
536 *Letters* **501**, 24–36 (2018).
- 537 31. J. C. Zachos, U. Röhl, S. A. Schellenberg, A. Sluijs, D. A. Hodell, D. C. Kelly, E. Thomas,
538 M. Nicolo, I. Raffi, L. J. Lourens, H. McCarren, D. Kroon, Paleoclimate: Rapid acidifica-
539 tion of the ocean during the paleocene-eocene thermal maximum. *Science* **308**, 1611–1615
540 (2005).
- 541 32. D. A. Harper, B. Cascales-Miñana, T. Servais, Early Palaeozoic diversifications and ex-
542 tinctions in the marine biosphere: A continuum of change. *Geol. Mag.* **157**, 5–21 (2020).

- 543 33. X. Zhou, E. Thomas, R. E. Rickaby, A. M. Winguth, Z. Lu, I/Ca evidence for upper ocean
544 deoxygenation during the PETM. *Paleoceanography* **29**, 964–975 (2014).
- 545 34. A. Sluijs, L. Van Roij, G. Harrington, S. Schouten, J. Sessa, L. LeVay, G.-J. Reichart,
546 C. Slomp, Warming, euxinia and sea level rise during the Paleocene–Eocene Thermal
547 Maximum on the Gulf Coastal Plain: implications for ocean oxygenation and nutrient
548 cycling. *Climate of the Past* **10**, 1421–1439 (2014).
- 549 35. V. Pujalte, J. Baceta, B. Schmitz, A massive input of coarse-grained siliciclastics in the
550 Pyrenean Basin during the PETM: the missing ingredient in a coeval abrupt change in
551 hydrological regime. *Climate of the Past* **11**, 1653–1672 (2015).
- 552 36. D. C. Kelly, J. C. Zachos, T. J. Bralower, S. A. Schellenberg, Enhanced terrestrial weath-
553 ering/runoff and surface ocean carbonate production during the recovery stages of the
554 Paleocene-Eocene thermal maximum. *Paleoceanography* **20** (2005).
- 555 37. R. Wicczorek, M. S. Fantle, L. R. Kump, G. Ravizza, Geochemical evidence for volcanic
556 activity prior to and enhanced terrestrial weathering during the Paleocene Eocene Thermal
557 Maximum. *Geochimica et Cosmochimica Acta* **119**, 391–410 (2013).
- 558 38. R. Speijer, C. Scheibner, P. Stassen, A.-M. M. Morsi, Response of marine ecosystems to
559 deep-time global warming: A synthesis of biotic patterns across the Paleocene-Eocene
560 thermal maximum (PETM). *Austrian Journal of Earth Sciences* **105**, 6–16 (2012).
- 561 39. M. R. Osburn, J. Owens, K. D. Bergmann, T. W. Lyons, Dynamic changes in sulfate sulfur
562 isotopes preceding the Ediacaran Shuram Excursion. *Geochim. Cosmochim. Acta* (2015).
- 563 40. S. J. Burns, A. Matter, Carbon isotopic record of the latest Proterozoic from Oman. *Eclo-
564 gae Geol. Helv.* **86**, 595–607 (1993).

- 565 41. E. Le Guerroué, P. A. Allen, A. Cozzi, Chemostratigraphic and sedimentological frame-
566 work of the largest negative carbon isotopic excursion in earth history: The neoproterozoic
567 Shuram formation (Nafun Group, Oman). *Precambrian Res.* **146**, 68–92 (2006).
- 568 42. Materials and methods are available as supplementary materials at the science advances
569 website .
- 570 43. A. Cozzi, P. A. Allen, J. P. Grotzinger, Understanding carbonate ramp dynamics using
571 $\delta^{13}\text{C}$ profiles: Examples from the Neoproterozoic Buah Formation of Oman. *Terra Nov.*
572 **16**, 62–67 (2004).
- 573 44. J. Wilcots, P. Gilbert, K. Bergmann, Nanoscale crystal fabric preserved in dolomite ooids
574 at the onset of the Ediacaran Shuram excursion. *Geophysical Research Letters* (PrePrint).
- 575 45. Y. Fang, H. Xu, Dissolved silica-catalyzed disordered dolomite precipitation. *American*
576 *Mineralogist: Journal of Earth and Planetary Materials* **107**, 443–452 (2022).
- 577 46. J. M. Husson, B. J. Linzmeier, K. Kitajima, A. Ishida, A. C. Maloof, B. Schoene, S. E.
578 Peters, J. W. Valley, Large isotopic variability at the micron-scale in ‘Shuram’ excursion
579 carbonates from South Australia. *Earth Planet. Sci. Lett.* **538** (2020).
- 580 47. A.-S. C. Ahm, C. J. Bjerrum, C. L. Blättler, P. K. Swart, J. A. Higgins, Quantifying early
581 marine diagenesis in shallow-water carbonate sediments. *Geochim. Cosmochim. Acta* **236**,
582 140–159 (2018).
- 583 48. N. Youbi, R. E. Ernst, U. Söderlund, M. A. Boumehdi, A. A. Lahna, C. C. G. Tassinari,
584 W. El Moume, M. K. Bensalah, The Central Iapetus magmatic province: An updated
585 review and link with the ca. 580 Ma Gaskiers glaciation. *Mass Extinctions, Volcanism,*
586 *and Impacts: New Developments* **544**, 35–66 (2020).

- 587 49. A. M. Andersson, A. Malehmir, V. R. Troll, M. Dehghannejad, M. Andersson,
588 A. Malehmir, V. R. Troll, M. Dehghannejad, C. Juhlin, M. Ask, Carbonatite ring-
589 complexes explained by caldera-style volcanism. *Sci. Rep.* **3**, 1–9 (2013).
- 590 50. M. Andersson, *3D Structure and Emplacement of the Alnö Alkaline and Carbonatite*
591 (2015).
- 592 51. A. G. Doroshkevich, G. S. Ripp, N. V. Vladykin, V. M. Savatenkov, Sources of the Late
593 Riphean carbonatite magmatism of Northern Transbaikalia: Geochemical and isotope-
594 geochemical data. *Geochemistry Int.* **49**, 1195–1207 (2011).
- 595 52. K. Secher, L. M. Heaman, T. F. D. Nielsen, S. M. Jensen, F. Schjøth, R. A. Creaser, Tim-
596 ing of kimberlite, carbonatite, and ultramafic lamprophyre emplacement in the alkaline
597 province located 64°-67° N in southern West Greenland. *Lithos* **112**, 400–406 (2009).
- 598 53. K. Attoh, F. Corfu, P. M. Nude, U-Pb zircon age of deformed carbonatite and alkaline
599 rocks in the Pan-African Dahomeyide suture zone, West Africa. *Precambrian Res.* **155**,
600 251–260 (2007).
- 601 54. K. Burke, L. D. Ashwal, S. J. Webb, New way to map old sutures using deformed alkaline
602 rocks and carbonatites. *Geology* **31**, 391–394 (2003).
- 603 55. A. B. Kampunzu, M. N. Makutu, G. Rocci, J. Kramers, F. Pineau, I. Louaradf, F. Tembo,
604 Neoproterozoic Alkaline and Carbonatite Magmatism Along the Western Rift in Central-
605 Eastern Africa: Break-up of Rodinia Supercontinent and Reconstruction of Gondwana.
606 *Gondwana Res.* **1**, 155–156 (1997).
- 607 56. J. J. Veevers, Pan-Gondwanaland post-collisional extension marked by 650-500 Ma alka-
608 line rocks and carbonatites and related detrital zircons: A review. *Earth-Science Rev.* **83**,
609 1–47 (2007).

- 610 57. C. Casquet, R. J. Pankhurst, C. Galindo, C. Rapela, C. M. Fanning, E. Baldo, J. Dahlquist,
611 J. M. G. Casado, F. Colombo, A deformed alkaline igneous rock-carbonatite complex
612 from the Western Sierras Pampeanas, Argentina: Evidence for late Neoproterozoic open-
613 ing of the Clymene Ocean? *Precambrian Res.* **165**, 205–220 (2008).
- 614 58. T. Paulsen, C. Deering, J. Sliwinski, O. Bachmann, M. Guillong, Evidence for a spike in
615 mantle carbon outgassing during the Ediacaran period. *Nature Geoscience* **10**, 930–934
616 (2017).
- 617 59. T. T. Isson, N. J. Planavsky, L. Coogan, E. Stewart, J. Ague, E. Bolton, S. Zhang,
618 N. McKenzie, L. Kump, Evolution of the global carbon cycle and climate regulation on
619 earth. *Global Biogeochemical Cycles* **34**, e2018GB006061 (2020).
- 620 60. K. D. Bergmann, J. Wilcots, T. Pico, N. Boekelheide, N. T. Anderson, M. D. Cantine, S. L.
621 Goldberg, B. Keller, A. B. Jost, A. Eyster, Onset of carbonate biomineralization drove
622 global reorganization of sedimentation and subsidence patterns. *Preprint at 10.1002/es-*
623 *soar.10511913.1* (2022).
- 624 61. B. Schmitz, V. Pujalte, Abrupt increase in seasonal extreme precipitation at the Paleocene-
625 Eocene boundary. *Geology* **35**, 215–218 (2007).
- 626 62. M. D. Cantine, J. B. Setera, J. A. VanTongeren, C. Mwinde, K. D. Bergmann, Grain
627 size and transport biases in an Ediacaran detrital zircon record. *Journal of Sedimentary*
628 *Research* **91**, 913–928 (2021).
- 629 63. K. Bergmann, J. Grotzinger, W. Fischer, Biological influences on seafloor carbonate pre-
630 cipitation. *Palaios* **28** (2013).

- 631 64. E. Dallanave, L. Tauxe, G. Muttoni, D. Rio, Silicate weathering machine at work: rock
632 magnetic data from the late Paleocene–early Eocene Cicogna section, Italy. *Geochemistry,*
633 *Geophysics, Geosystems* **11** (2010).
- 634 65. C. Robert, J. P. Kennett, Antarctic subtropical humid episode at the Paleocene-Eocene
635 boundary: clay-mineral evidence. *Geology* **22**, 211–214 (1994).
- 636 66. X. Chen, Y. Zhou, G. A. Shields, Progress towards an improved Precambrian seawater
637 $^{87}\text{Sr}/^{86}\text{Sr}$ curve. *Earth-Science Reviews* **224**, 103869 (2022).
- 638 67. J. C. Walker, P. B. Hays, J. F. Kasting, A negative feedback mechanism for the long-term
639 stabilization of Earth’s surface temperature. *J. Geophys. Res.* **86**, 9776–9782 (1981).
- 640 68. A. J. Ridgwell, Carbonate Deposition, Climate Stability, and Neoproterozoic Ice Ages.
641 *Science* **302**, 859–862 (2003).
- 642 69. A. D. Rooney, M. D. Cantine, K. D. Bergmann, I. Gómez-Pérez, B. A. Baloushi, T. H.
643 Boag, J. F. Busch, E. A. Sperling, J. V. Strauss, Calibrating the coevolution of Ediacaran
644 life and environment. *Proc. Natl. Acad. Sci. U. S. A.* **117**, 16824–16830 (2020).
- 645 70. G. Jiang, X. Wang, X. Shi, S. Xiao, S. Zhang, J. Dong, The origin of decoupled carbonate
646 and organic carbon isotope signatures in the early Cambrian (ca. 542-520Ma) Yangtze
647 platform. *Earth Planet. Sci. Lett.* **317-318**, 96–110 (2012).
- 648 71. C. Lee, G. D. Love, W. W. Fischer, J. P. Grotzinger, G. P. Halverson, Marine organic
649 matter cycling during the Ediacaran Shuram excursion. *Geology* **43**, 1103–1106 (2015).
- 650 72. C. Lee, D. A. Fike, G. D. Love, A. L. Sessions, J. P. Grotzinger, R. E. Summons, W. W.
651 Fischer, Carbon isotopes and lipid biomarkers from organic-rich facies of the Shuram
652 Formation, Sultanate of Oman. *Geobiology* **11**, 406–419 (2013).

- 653 73. L. A. Riedman, P. M. Sadler, Global species richness record and biostratigraphic potential
654 of early to middle Neoproterozoic eukaryote fossils. *Precambrian Res.* **319**, 6–18 (2018).
- 655 74. C. Yang, A. D. Rooney, D. J. Condon, X.-H. Li, D. V. Grazhdankin, F. T. Bowyer, C. Hu,
656 F. A. Macdonald, M. Zhu, The tempo of Ediacaran evolution. *Science Advances* **7**,
657 eabi9643 (2021).
- 658 75. F. Zhang, H. Wang, Y. Ye, Y. Liu, Y. Lyu, Y. Deng, D. Lyu, X. Wang, H. Wu, S. Deng,
659 *et al.*, Did high temperature rather than low O₂ hinder the evolution of eukaryotes in the
660 Precambrian? *Precambrian Research* **378**, 106755 (2022).
- 661 76. S. Xiao, B. Shen, Q. Tang, A. J. Kaufman, X. Yuan, J. Li, M. Qian, Biostratigraphic and
662 chemostratigraphic constraints on the age of early Neoproterozoic carbonate successions
663 in North China. *Precambrian Res.* **246**, 208–225 (2014).
- 664 77. K. A. McFadden, J. Huang, X. Chu, G. Jiang, A. J. Kaufman, C. Zhou, X. Yuan, S. Xiao,
665 Pulsed oxidation and biological evolution in the Ediacaran Doushantuo Formation. *Proc.*
666 *Natl. Acad. Sci.* **105**, 3197–3202 (2008).
- 667 78. N. J. Butterfield, J. P. Grotzinger, Palynology of the Huqf Supergroup, Oman. *Geol. Soc.*
668 *London, Spec. Publ.* **366**, 251–263 (2012).
- 669 79. S. Xiao, G. M. Narbonne, C. Zhou, M. Laflamme, D. V. Grazhdankin, M. Moczydlowska-
670 Vidal, H. Cui, Towards an Ediacaran time scale: Problems, protocols, and prospects.
671 *Episodes* **39**, 540–555 (2016).
- 672 80. Z. An, G. Jiang, J. Tong, L. Tian, Q. Ye, H. Song, H. Song, Stratigraphic position of
673 the Ediacaran Miaohe biota and its constrains on the age of the upper Doushantuo $\delta^{13}\text{C}$
674 anomaly in the Yangtze Gorges area, South China. *Precambrian Res.* **271**, 243–253
675 (2015).

- 676 81. H. Song, D. B. Kemp, L. Tian, D. Chu, H. Song, X. Dai, Thresholds of temperature change
677 for mass extinctions. *Nature communications* **12**, 1–8 (2021).
- 678 82. T. H. Boag, R. G. Stockey, L. E. Elder, P. M. Hull, E. A. Sperling, Oxygen, temperature
679 and the deep-marine stenothermal cradle of Ediacaran evolution. *Proc. R. Soc. B Biol. Sci.*
680 **285**, 20181724 (2018).
- 681 83. C. Simpson, Adaptation to a viscous Snowball Earth ocean as a path to complex multice-
682 lularity. *The American Naturalist* **198**, 590–609 (2021).
- 683 84. S. T. Kim, J. R. O’Neil, Equilibrium and nonequilibrium oxygen isotope effects in syn-
684 thetic carbonates. *Geochim. Cosmochim. Acta* **61**, 3461–3475 (1997).
- 685 85. J. Horita, Oxygen and carbon isotope fractionation in the system dolomite–water–CO₂ to
686 elevated temperatures. *Geochim. Cosmochim. Acta* **129**, 111–124 (2014).
- 687 86. T. Ishikawa, Y. Ueno, T. Komiya, Y. Sawaki, J. Han, D. Shu, Y. Li, S. Maruyama,
688 N. Yoshida, Carbon isotope chemostratigraphy of a Precambrian/Cambrian boundary sec-
689 tion in the Three Gorge area, South China: Prominent global-scale isotope excursions just
690 before the Cambrian Explosion. *Gondwana Res.* **14**, 193–208 (2008).
- 691 87. R. Kikumoto, M. Tahata, M. Nishizawa, Y. Sawaki, S. Maruyama, D. Shu, J. Han,
692 T. Komiya, K. Takai, Y. Ueno, Nitrogen isotope chemostratigraphy of the Ediacaran and
693 Early Cambrian platform sequence at Three Gorges, South China. *Gondwana Res.* **25**,
694 1057–1069 (2014).
- 695 88. J. P. Pu, S. A. Bowring, J. Ramezani, P. Myrow, T. D. Raub, E. Landing, A. Mills, E. Hod-
696 gin, F. A. Macdonald, Dodging snowballs: Geochronology of the Gaskiers glaciation and
697 the first appearance of the Ediacaran biota. *Geology* **44**, 955–958 (2016).

- 698 89. Y. Sawaki, T. Ohno, M. Tahata, T. Komiya, T. Hirata, S. Maruyama, B. F. Windley, J. Han,
699 D. Shu, Y. Li, The Ediacaran radiogenic Sr isotope excursion in the Doushantuo Formation
700 in the Three Gorges area, South China. *Precambrian Res.* **176**, 46–64 (2010).
- 701 90. D. A. Fike, J. P. Grotzinger, L. M. Pratt, R. E. Summons, Oxidation of the Ediacaran
702 ocean. *Nature* **444**, 744–747 (2006).
- 703 91. C. Li, D. S. Hardisty, G. Luo, J. Huang, T. J. Algeo, M. Cheng, W. Shi, Z. An, J. Tong,
704 S. Xie, N. Jiao, T. W. Lyons, Uncovering the spatial heterogeneity of Ediacaran carbon
705 cycling. *Geobiology* **15**, 211–224 (2017).
- 706 92. B. G. Pokrovskii, V. A. Melezhik, M. I. Bujakaite, Carbon, oxygen, strontium, and sulfur
707 isotopic compositions in late Precambrian rocks of the Patom Complex, central Siberia:
708 Communication 1. results, isotope stratigraphy, and dating problems. *Lithol. Miner. Re-*
709 *sour.* **41**, 450–474 (2006).
- 710 93. M. Tahata, Y. Ueno, T. Ishikawa, Y. Sawaki, K. Murakami, J. Han, D. Shu, Y. Li, J. Guo,
711 N. Yoshida, T. Komiya, Carbon and oxygen isotope chemostratigraphies of the Yangtze
712 platform, South China: Decoding temperature and environmental changes through the
713 Ediacaran. *Gondwana Res.* **23**, 333–353 (2013).
- 714 94. X. Wang, G. Jiang, X. Shi, S. Xiao, Paired carbonate and organic carbon isotope variations
715 of the Ediacaran Doushantuo Formation from an upper slope section at Siduping, South
716 China. *Precambrian Res.* **273**, 53–66 (2016).
- 717 95. G. M. Cox, G. P. Halverson, A. Poirier, D. Le Heron, J. V. Strauss, R. Stevenson, A model
718 for Cryogenian iron formation. *Earth Planet. Sci. Lett.* **433**, 280–292 (2016).
- 719 96. P. C. Boggiani, C. Gaucher, A. N. Sial, M. Babinski, C. M. Simon, C. Riccomini, V. P.
720 Ferreira, T. R. Fairchild, Chemostratigraphy of the Tamengo Formation (Corumbá Group,

- 721 Brazil): A contribution to the calibration of the Ediacaran carbon-isotope curve. *Precam-*
722 *brian Res.* **182**, 382–401 (2010).
- 723 97. J. J. Veevers, Pan-Gondwanaland post-collisional extension marked by 650-500 Ma alka-
724 line rocks and carbonatites and related detrital zircons: A review. *Earth-Science Rev.* **83**,
725 1–47 (2007).
- 726 98. R. E. Ernst, K. L. Buchan, Large mafic magmatic events through time and links to mantle-
727 plume heads. *Spec. Pap. Geol. Soc. Am.* **352**, 483–575 (2001).
- 728 99. R. E. Ernst, K. Bell, Large igneous provinces (LIPs) and carbonatites. *Mineral. Petrol.* **98**,
729 55–76 (2010).
- 730 100. A. R. Woolley, B. a. Kjarsgaard, Carbonatite Occurrences of the World :. *Nat. Hist.* (2008).
- 731 101. D. Li, H. F. Ling, G. A. Shields-Zhou, X. Chen, L. Cremonese, L. Och, M. Thirlwall,
732 C. J. Manning, Carbon and strontium isotope evolution of seawater across the Ediacaran-
733 Cambrian transition: Evidence from the Xiaotan section, NE Yunnan, South China. *Pre-*
734 *cambrian Res.* **225**, 128–147 (2013).
- 735 102. J. P. Hodych, R. A. Cox, Ediacaran U–Pb zircon dates for the Lac Matapédia and Mt.
736 St.-Anselme basalts of the Quebec Appalachians: support for a long-lived mantle plume
737 during the rifting phase of Iapetus opening. *Can J Earth Sci* **581**, 565–581 (2007).
- 738 103. K. Secher, L. M. Heaman, T. F. D. Nielsen, S. M. Jensen, F. Schjøth, R. A. Creaser, Tim-
739 ing of kimberlite, carbonatite, and ultramafic lamprophyre emplacement in the alkaline
740 province located 64°-67° N in southern West Greenland. *Lithos* **112**, 400–406 (2009).
- 741 104. E. McClellan, E. Gazel, The Cryogenian intra-continental rifting of Rodinia: Evidence
742 from the Laurentian margin in eastern North America. *Lithos* **206-207**, 321–337 (2014).

- 743 105. S. Tappe, A. Steinfeld, T. Nielsen, Asthenospheric source of Neoproterozoic and Mesozoic
744 kimberlites from the North Atlantic craton, West Greenland: New high-precision U-Pb
745 and Sr-Nd isotope data on perovskite. *Chem. Geol.* **320-321**, 113–127 (2012).
- 746 106. J. G. Meert, T. H. Torsvik, The making and unmaking of a supercontinent: Rodinia revis-
747 ited. *Tectonophysics* **375**, 261–288 (2003).
- 748 107. C. R. Calver, L. P. Black, J. L. Everard, D. B. Seymour, U-Pb zircon age constraints on
749 late Neoproterozoic glaciation in Tasmania. *Geology* **32**, 893–896 (2004).
- 750 108. C. R. Calver, J. L. Crowley, M. T. Wingate, D. A. Evans, T. D. Raub, M. D. Schmitz, Glob-
751 ally synchronous marinoan deglaciation indicated by U-Pb geochronology of the cottons
752 Breccia, Tasmania, Australia. *Geology* **41**, 1127–1130 (2013).
- 753 109. S. Meffre, N. G. Direen, A. J. Crawford, V. Kamenetsky, Mafic volcanic rocks on King
754 Island, Tasmania: Evidence for 579 Ma break-up in east Gondwana. *Precambrian Res.*
755 **135**, 177–191 (2004).
- 756 110. K. Attoh, F. Corfu, P. M. Nude, U-Pb zircon age of deformed carbonatite and alkaline
757 rocks in the Pan-African Dahomeyide suture zone, West Africa. *Precambrian Res.* **155**,
758 251–260 (2007).
- 759 111. E. Eneroth, O. M. Sverningsen, Equatorial Baltica in the Vendian: Palaeomagnetic data
760 from the Sarek Dyke Swarm, northern Swedish Caledonides. *Precambrian Res.* **129**, 23–
761 45 (2004).
- 762 112. D. P. Gladkochub, S. A. Pisarevsky, T. V. Donskaya, R. E. Ernst, M. T. D. Wingate,
763 U. Soderlund, A. M. Mazukabzov, E. V. Sklyarov, M. A. Hamilton, J. A. Hanes, Protero-
764 zoic mafic magmatism in Siberian craton: An overview and implications for paleoconti-
765 nental reconstruction. *Precambrian Res.* **183**, 660–668 (2010).

- 766 113. V. Yarmolyuk, V. Kovalenko, E. Salnikova, A. Nikiforov, A. Kotov, N. Vladykin, *DOK-*
767 *LADY EARTH SCIENCES C/C OF DOKLADY-AKADEMIIA NAUK* (INTERPERIOD-
768 ICA PUBLISHING, 2006), vol. 404, p. 1031.
- 769 114. D. V. Metelkin, V. A. Vernikovskiy, A. Y. Kazansky, Neoproterozoic evolution of Rodinia:
770 constraints from new paleomagnetic data on the western margin of the Siberian craton.
771 *Russ. Geol. Geophys.* **48**, 32–45 (2007).
- 772 115. N. V. Vladykin, A. B. Kotov, A. S. Borisenko, V. V. Yarmolyuk, N. P. Pokhilenko, E. B.
773 Sal'nikova, A. V. Travin, S. Z. Yakovleva, Age boundaries of formation of the Tomtor
774 alkaline-ultramafic pluton: U-Pb and ⁴⁰Ar/³⁹Ar geochronological studies. *Dokl. Earth*
775 *Sci.* **454**, 7–11 (2014).
- 776 116. V. V. Vrublevskii, V. V. Reverdatto, a. E. Izokh, I. F. Gertner, D. S. Yudin, P. a. Tishin,
777 Neoproterozoic carbonatite magmatism of the Yenisei Ridge, Central Siberia: ⁴⁰Ar/³⁹Ar
778 geochronology of the Penchenga rock complex. *Dokl. Earth Sci.* **437**, 443–448 (2011).
- 779 117. J. P. Donatti-Filho, S. Tappe, E. P. Oliveira, L. M. Heaman, Age and origin of the Neopro-
780 terozoic Brauna kimberlites: Melt generation within the metasomatized base of the São
781 Francisco craton, Brazil. *Chemical Geology* **353**, 19–35 (2013).
- 782 118. A. D. Nozhkin, O. M. Turkina, T. B. Bayanova, N. G. Berezhnaya, A. N. Larionov, A. A.
783 Postnikov, A. V. Travin, R. E. Ernst, Neoproterozoic rift and within-plate magmatism in
784 the Yenisei Ridge: implications for the breakup of Rodinia. *Russ. Geol. Geophys.* **49**,
785 503–519 (2008).
- 786 119. a. E. Vernikovskaya, V. M. Datsenko, V. a. Vernikovskiy, N. Y. Matushkin, Y. M. Laevsky,
787 I. V. Romanova, a. V. Travin, K. V. Voronin, E. N. Lepekhina, Magmatism evolution
788 and carbonatite-granite association in the neoproterozoic active continental margin of the

- 789 Siberian craton: Thermochronological reconstructions. *Dokl. Earth Sci.* **448**, 161–167
790 (2013).
- 791 120. F. V. Kaminsky, S. M. Sablukov, L. I. Sablukova, D. M. D. Channer, Neoproterozoic
792 'anomalous' kimberlites of Guaniamo, Venezuela: Mica kimberlites of 'isotopic transi-
793 tional' type. *Lithos* **76**, 565–590 (2004).
- 794 121. S. W. Denyszyn, H. C. Halls, D. W. Davis, D. A. Evans, Paleomagnetism and U-Pb
795 geochronology of Franklin dykes in high arctic Canada and Greenland: A revised age
796 and paleomagnetic pole constraining block rotations in the Nares Strait region. *Can. J.*
797 *Earth Sci.* **46**, 689–705 (2009).
- 798 122. A. A. Ariskin, Y. A. Kostitsyn, E. G. Konnikov, L. V. Danyushevsky, S. Meffre, G. S.
799 Nikolaev, A. McNeill, E. V. Kislov, D. A. Orsoev, Geochronology of the Dovyren intrusive
800 complex, northwestern Baikal area, Russia, in the Neoproterozoic. *Geochemistry Int.* **51**,
801 859–875 (2013).
- 802 123. Z.-X. Li, S. Bogdanova, A. Collins, A. Davidson, B. De Waele, R. Ernst, I. Fitzsimons,
803 R. Fuck, D. Gladkochub, J. Jacobs, *et al.*, Assembly, configuration, and break-up history
804 of Rodinia: a synthesis. *Precambrian research* **160**, 179–210 (2008).
- 805 124. C. Li, P. Peng, G. Sheng, J. Fu, Y. Yan, A molecular and isotopic geochemical study
806 of Meso- to Neoproterozoic (1.73-0.85 Ga) sediments from the Jixian section, Yanshan
807 Basin, North China. *Precambrian Res.* **125**, 337–356 (2003).
- 808 125. J. K. Park, K. L. Buchan, S. S. Harlan, A proposed giant radiating dyke swarm fragmented
809 by the separation of Laurentia and Australia based on paleomagnetism of ca. 780 Ma mafic
810 intrusions in western North America. *Earth Planet. Sci. Lett.* **132**, 129–139 (1995).

- 811 126. Y. Zhang, D. A. Rodionov, M. S. Gelfand, V. N. Gladyshev, Comparative genomic analy-
812 ses of nickel, cobalt and vitamin B12 utilization. *BMC Genomics* **10**, 78 (2009).
- 813 127. C. L. Zhang, X. H. Li, Z. X. Li, S. N. Lu, H. M. Ye, H. M. Li, Neoproterozoic ultramafic-
814 mafic-carbonatite complex and granitoids in Quruqtagh of northeastern Tarim Block,
815 western China: Geochronology, geochemistry and tectonic implications. *Precambrian*
816 *Res.* **152**, 149–169 (2007).
- 817 128. A. Fabris, S. Constable, C. Conor, A. Woodhouse, S. Hore, M. Fanning, Age, origin,
818 emplacement and mineral potential of the Oodla Wirra Volcanics, Nackara Arc, central
819 Flinders Ranges. *MESA J.* **37**, 44–52 (2005).
- 820 129. T. H. Boag, S. A. Darroch, M. Laflamme, Ediacaran distributions in space and time: Test-
821 ing assemblage concepts of earliest macroscopic body fossils. *Paleobiology* **42**, 574–594
822 (2016).
- 823 130. M. Foote, Origination and extinction components of taxonomic diversity: general prob-
824 lems. *Paleobiology* **26**, 74–102 (2000).
- 825 131. J. P. Grotzinger, Upward shallowing platform cycles: a response to 2.2 billion years of
826 low-amplitude, high-frequency (Milankovitch band) sea level oscillations. *Paleoceanog-*
827 *raphy* **1**, 403–416 (1986).
- 828 132. A. Cozzi, J. P. Grotzinger, P. A. Allen, Evolution of a terminal Neoproterozoic carbonate
829 ramp system (Buah Formation, Sultanate of Oman): Effects of basement paleotopography.
830 *Bull. Geol. Soc. Am.* **116**, 1367–1384 (2004).
- 831 133. A. C. Ries, R. M. Shackleton, Structures in the Huqf-Haushi Uplift, east Central Oman.
832 *Geol. Soc. London, Spec. Publ.* **49**, 653–663 (1990).

- 833 134. V. P. Wright, A. C. Ries, S. G. Munn, Intraplatformal basin-fill deposits from the Infra-
834 cambrian Huqf Group, east central Oman. *Geol. Soc. London, Spec. Publ.* **49**, 601–616
835 (1990).
- 836 135. G. E. Gorin, L. G. Racz, M. R. Walter, Late Precambrian-Cambrian sediments of Huqf
837 Group, Sultanate of Oman. *Am. Assoc. Pet. Geol. Bull.* **66**, 2609–2627 (1982).
- 838 136. J. Dubreuilh, J. P. Platel, J. Le Métour, J. Roger, R. Wyns, F. Béchenec, A. Berthiaux,
839 Explanatory notes to the Geological map of Khaluf, Sheet NF 40-15, scale 1: 250000,
840 *Tech. rep.*, Directorate General of minerals, Oman ministry of petroleum and minerals
841 (1992).
- 842 137. G. D. Love, E. Grosjean, C. Stalvies, D. a. Fike, J. P. Grotzinger, A. S. Bradley, A. E. Kelly,
843 M. Bhatia, W. Meredith, C. E. Snape, S. a. Bowring, D. J. Condon, R. E. Summons, Fossil
844 steroids record the appearance of Demospongiae during the Cryogenian period. *Nature*
845 **457**, 718–21 (2009).
- 846 138. E. Grosjean, G. D. Love, C. Stalvies, D. A. Fike, R. E. Summons, Origin of petroleum in
847 the Neoproterozoic–Cambrian South Oman Salt Basin. *Org. Geochem.* (2009).
- 848 139. J. D. Hemingway, G. A. Henkes, A disordered kinetic model for clumped isotope bond
849 reordering in carbonates. *Earth and Planetary Science Letters* **566**, 116962 (2021).
- 850 140. D. A. Stolper, J. M. Eiler, The kinetics of solid-state isotope-exchange reactions for
851 clumped isotopes: A study of inorganic calcites and apatites from natural and experi-
852 mental samples. *Am. J. Sci.* **315**, 363–411 (2015).
- 853 141. G. A. Henkes, B. H. Passey, E. L. Grossman, B. J. Shenton, A. Perez-Huerta, T. E. Yancey,
854 Temperature limits for preservation of primary calcite clumped isotope paleotemperatures.
855 *Geochim. Cosmochim. Acta* **139**, 362–382 (2014).

- 856 142. M. K. Lloyd, J. M. Eiler, P. I. Nabelek, Clumped isotope thermometry of calcite and
857 dolomite in a contact metamorphic environment. *Geochim. Cosmochim. Acta* **197**, 323–
858 344 (2017).
- 859 143. M. Bonifacie, D. Calmels, J. Eiler, Clumped Isotope Thermometry of Marbles as an In-
860 dicator of the Closure Temperatures of Calcite and Dolomite with Respect to Solid-State
861 Reordering of C–O Bonds. *Mineral. Mag.* **77**, 735 (2013).
- 862 144. W. Visser, Burial and thermal history of Proterozoic source rocks in Oman. *Precambrian*
863 *Res.* **54**, 15–36 (1991).
- 864 145. M. G. McCarron, The sedimentology and chemostratigraphy of the Nafun Group, Huqf
865 Supergroup, Oman, Phd thesis, Oxford University (1999).
- 866 146. K. D. T. Nguyen, S. A. Morley, C. H. Lai, M. S. Clark, K. S. Tan, A. E. Bates, L. S. Peck,
867 Upper temperature limits of tropical marine ectotherms: Global warming implications.
868 *PLoS One* **6** (2011).

869 **Acknowledgements:** K.D.B. thanks John Grotzinger for initial support with the geol-
870 ogy of Oman and John Eiler for support with the clumped isotope measurements published
871 in (16). Both provided feedback on early versions of this manuscript. C. Ma, J. Hurowitz,
872 N. Kitchen, and Y. Guan provided assistance with analytical measurements. JC Creveling,
873 Dave Johnston, and Andy Knoll provided feedback on early versions of this manuscript. Por-
874 tions of this research were carried out at the Stanford Synchrotron Radiation Lightsource, a
875 Directorate of SLAC National Accelerator Laboratory and an Office of Science User Facil-
876 ity operated for the US Department of Energy Office of Science by Stanford University. S.
877 Webb and J. Johnson helped with the XANES measurements at SLAC and provided standard
878 data. We thank Petroleum Development Oman employees for helpful discussions, particularly
879 Irene Gomez Perez, Joachim Amthor, Gideon Lopes Cardozo, Erwin Adams, Gordon Forbes,
880 Badar Al Balushi, and Sven Scholten. Funding for analytical measurements was provided by
881 the Agouron Institute and NASA Astrobiology Institute. We thank the Ministry of Energy
882 and Minerals of the Sultanate of Oman and Petroleum Development Oman for permission to
883 publish this manuscript and for fieldwork and analytical support. Thure Cerling, Lou Derry,
884 and an anonymous reviewer provided helpful criticism of an earlier version of this manuscript.
885 **Funding:** K.D.B. acknowledges funding from the Packard Foundation and NASA Exobiology
886 Grant 80NSSC19K0464. M.D.C. was supported by a National Defense Science and Engineer-
887 ing Graduate Fellowship; K.D.B. and M.R.O. were supported by National Science Foundation
888 Graduate Research Fellowships during their PhDs; **Author Contributions:** K.D.B. and W.F.
889 conceptualized the study. K.D.B., M.R.O., and M.D.C. conducted field investigations. K.D.B.,
890 N.B., and J.W. contributed formal analysis, software, and visualization. K.D.B. wrote the orig-
891 inal draft. All authors reviewed and edited the manuscript; **Data and materials availability:**
892 All data are provided in the main text or in the supplementary materials. Data, figures, and
893 code are available at Open Science Framework (link) for reviewers and will be made publicly

894 available on manuscript acceptance.

895 **Supplementary Materials** :

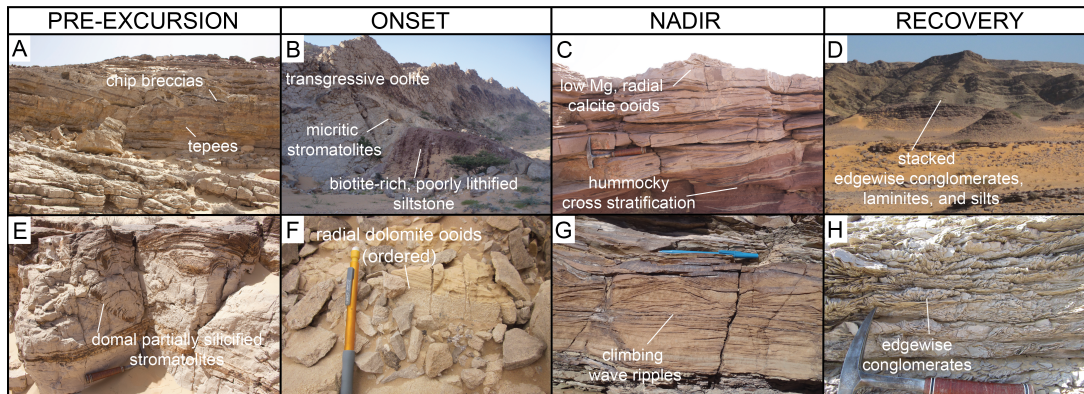
896 Materials and Methods

897 Figs. S1 - S9

898 References (83 - 146)

TEST	CLIMATE	DIAGENETIC MODELS			
	<i>this study</i>	<i>Deep Burial (Derry et al., 2010)</i>	<i>Authigenic (Schrag et al., 2013)</i>	<i>Meteoric (Knauth & Kennedy, 2008)</i>	<i>Selective (Higgins et al., 2018)</i>
SEDIMENT- OLOGY & STRATIGRA- PHY	reflect environmental & climatic change	coarsely crystalline	authigenic phases like nodules and concretions	coarsely crystalline	coarsely crystalline in low Sr intervals
PETROGRAPHY	well preserved phases precipitated from seawater	dissolution- large crystals	authigenic carbonate	dissolution- reprecipitation, leaching	dissolution- reprecipitation within low Sr intervals
MINERALOGY	controlled by pH and alkalinity of seawater	no prediction	no prediction	aragonite to calcite	sediment- buffered interval keeps high Sr
TRACE ELEMENTS	distinct across petrographic phases	homogenized	distinct in authigenic phase	homogenized	homogenized within low Sr interval
ISOTOPIC VARIABILITY	homogenous from DIC reservoir	homogenized	¹³ C distinct in authigenic phase	homogenized	homogenized within low Sr interval
TEMPERATURE AND FLUID $\delta^{18}\text{O}$ COMPOSITION	warming during excursion, marine $\delta^{18}\text{O}$	high burial T, heavy fluid $\delta^{18}\text{O}$	moderate T, marine $\delta^{18}\text{O}$	low T, meteoric $\delta^{18}\text{O}$	T and fluid $\delta^{18}\text{O}$ vary
BURIAL ENVIRONMENT	sediment- buffered	sediment- buffered	sediment- buffered	fluid-buffered	fluid- and sediment- buffered intervals

900 **Table 1. Proposed models of the Shuram excursion** Tests of previous (diagenetic) and pro-
901 posed (climate) mechanisms for the Shuram excursion using a variety of observations.



903 **Fig. 1. The stratigraphic expression of the Shuram excursion in the Huqf region of Oman**

904 (A, E) Pre-excursion peritidal dolomite facies including stromatolites, tepees, chip breccias.

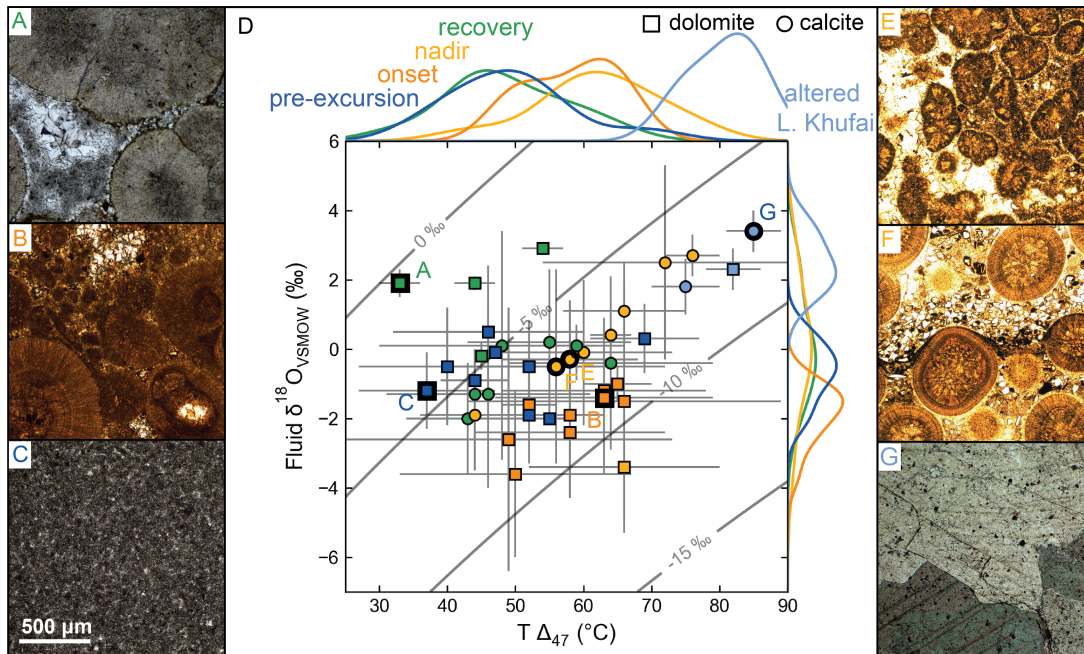
905 (B, F) transgressive dolomitic oolite capped by micritic stromatolites and red silts. (C) Cross-

906 stratified calcitic oolite capping red siltstones of the Shuram Formation. (D, H) Stacked storm-

907 derived edgewise conglomerates, silts, and crinkly laminites at Mukhaibah Dome. (G) Outer

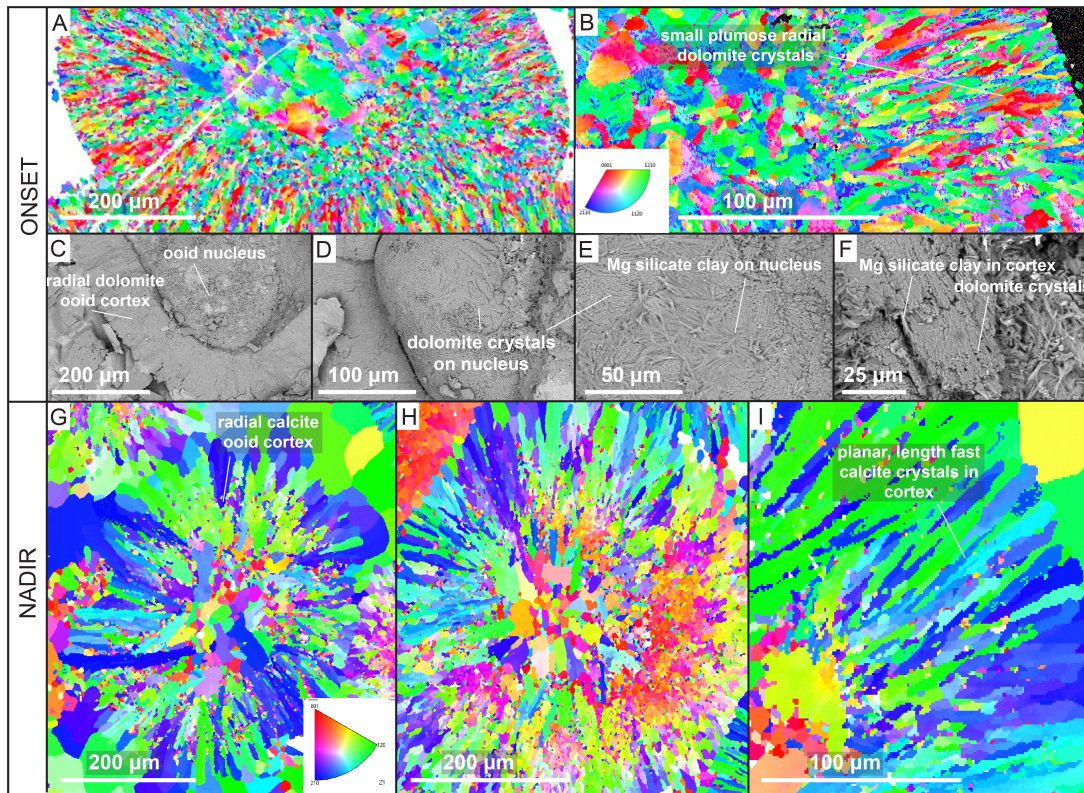
908 shelf Shuram Formation carbonate beds with climbing wave ripples in green siltstones of the

909 Oman Mountains.



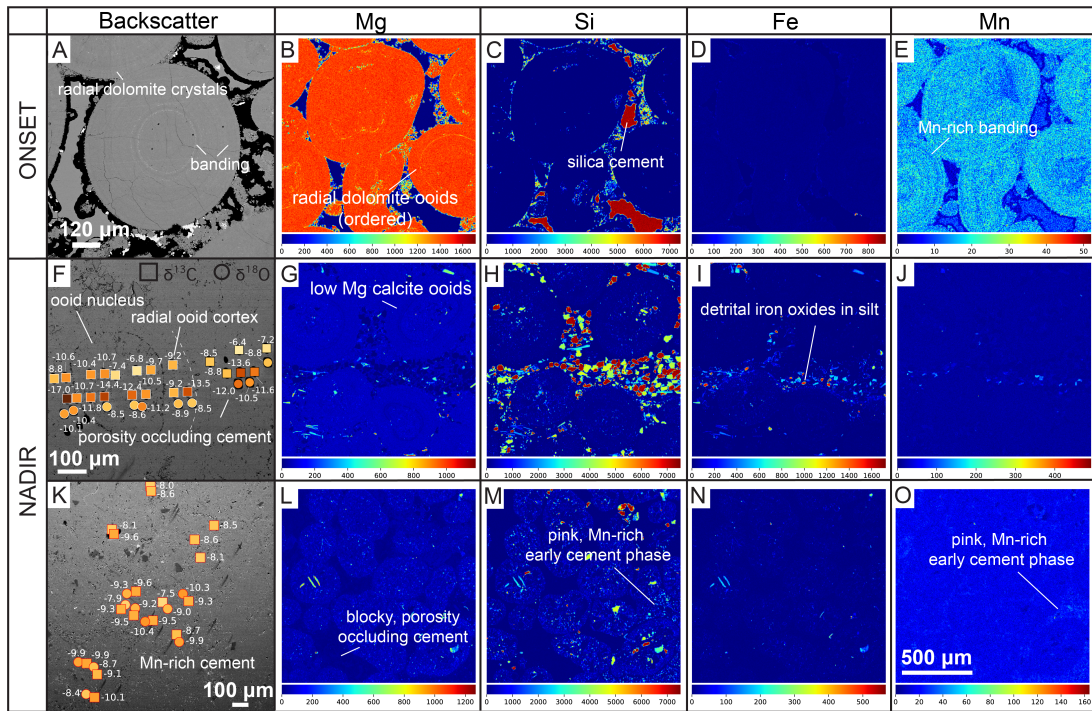
910

911 **Fig. 2. Petrographic character and burial alteration environment of inner shelf carbonates**
 912 **hosting the excursion (A)** Thin-section photomicrograph of dolomitic conophyton stromato-
 913 lite from the recovery of the excursion. **(B)** Dolomitic oolite hosting the onset of the excursion
 914 with silica cement under cross polarized light. **(C)** Mudstone from the pre-excursion peritidal
 915 Upper Khufai Fm. **(D)** Clumped isotope temperature vs. calculated water $\delta^{18}\text{O}_{VSMOW}$ with
 916 isopleths of carbonate $\delta^{18}\text{O}_{VPDB}$. The populations all tend to along $\delta^{18}\text{O}_{VPDB}$ isopleths indi-
 917 cating sediment-buffered alteration. Both the onset and nadir populations are warmer than the
 918 populations of pre-excursion and recovery. **(E)** Calcitic oolite from the nadir of the excursion
 919 with two distinct cement phases (early Mn-rich cement and later blocky cement). **(F)** Calcitic
 920 oolite from the nadir of the excursion intercalated with silt. **(G)** Coarsely recrystallized calcite
 921 from the lower Khufai Formation. The scale bar applies to all images.



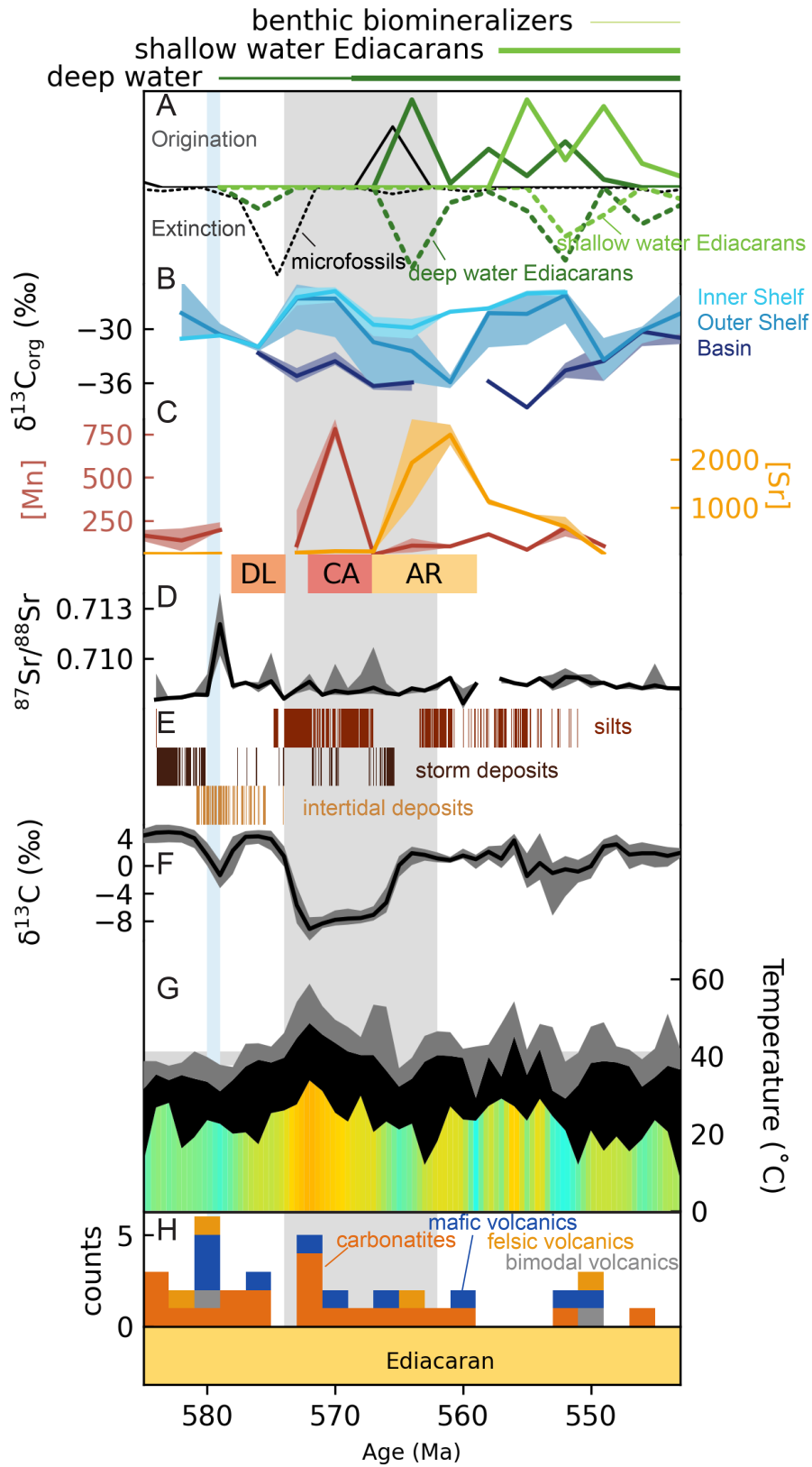
922

923 **Fig. 3. Mineralogy and crystal orientation of dolomite and calcite ooids recording the**
 924 **excursion. (A, B) Electron backscatter diffraction (EBSD) crystal orientation maps of dolomite**
 925 **ooids from the onset of the excursion with radial crystal orientations in the cortex, see also (44).**
 926 **(C, D, E, F) SEM images of cryo-fractured dolomite ooids with a Mg silicate clay in both the**
 927 **nucleus and cortex. (G, H, I) EBSD crystal orientation maps of calcite ooids from the nadir.**



928

929 **Fig. 4. In situ isotopic and trace metal variations.** (A) SEM backscatter images of dolomite
 930 ooids from the onset of the excursion. (B, C, D, E) Elemental maps of Mg, Si, Fe and Mn.
 931 Visible silica cement as in Fig. 2B. (F, K) SEM backscatter images of calcite ooids from the
 932 nadir of the excursion with SIMS spot analyses of carbon (squares) and oxygen (circles) isotopic
 933 composition of ooids (white outline), blocky cement (black outline), and early Mn-rich cement
 934 (red outline). (G, H, I, J, L, M, N, O) Respective elemental maps of each nadir oolite. Visible
 935 detrital minerals around the ooids include quartz, biotite, and iron and titanium oxides. Scale
 936 bar on the elemental map applies to all maps.



938 **Fig. 5. Evidence for a coupled climate-carbon cycle perturbation.** (A) Extinction and orig-
939 ination based on fossil occurrence data in 3 Myr bins (42). (B) $\delta^{13}\text{C}_{org}$ from three depositional
940 environments in Oman and China. (C) Composite Mn and Sr (ppm) records and suggested pri-
941 mary mineralogies dominating shallow marine environments through time (DL: dolomite, CA:
942 calcite, AR: aragonite). (D) $^{87}\text{Sr}/^{86}\text{Sr}$ from (66). (E) Sedimentologic evidence for silt, storm
943 deposits, and intertidal deposits in Central Oman. (F) $\delta^{13}\text{C}$ composite record. (G) Composite
944 temperature ($^{\circ}\text{C}$ record excluding Ediacaran sites from Laurentia and Russia. The 1st to 25th
945 quantiles (black) and 25th to 50th quantiles (grey) of shallow marine temperatures estimated
946 from $\delta^{18}\text{O}$ using quantile regression on points within 1 Myr windows sampled each 1 Myr. (H)
947 Counts of extrusive volcanic provinces. Blue line marks the Gaskiers glaciation. Grey band is
948 the approximate duration of the Shuram excursion. The shaded regions in B, C, D, and F are the
949 25th to 75th quantiles and median using quantile regression on points within 1 Myr windows
950 sampled each 1 Myr (D, F) or within 3 Myr windows sampled each 3 Myr (B, C). (42).

951 **Supplementary Materials for: The Shuram excursion: A response to climate extremes at**
952 **the dawn of animal life**

953 Authors:

954 Kristin D. Bergmann, Magdalena Osburn, Julia Wilcots,

955 Marjorie Cantine, Nicholas Boekelheide Woodward W. Fischer,

956 Magali Bonifacie

957 **1 Materials and Methods**

958 **Stratigraphic measurement, sample collection and preparation** Carbonate samples were
959 collected from outcrop locations from the Huqf Outcrop area in the winters of 2010 and 2011.
960 Stratigraphic sections were measured and sampled in stratigraphic height at Mukhaibah Dome
961 (MD) and Khufai Dome (KD) in the Huqf Outcrop area. Hand samples were cut to expose an
962 unweathered face prior to further sampling or analysis. A variety of lithofacies were analyzed
963 from each stratigraphic section including mudstone, stromatolite boundstone, oolitic grainstone,
964 siltstone, sandstone and edgewise conglomerate and features like tepees. The textural range
965 sampled was in part driven by necessity because no single facies persists through the entire
966 excursion at high resolution. The added benefit of analyzing a range of carbonate facies is an
967 improved understanding of preservation biases associated with specific carbonate textures and
968 different primary porosities that lead to varying contributions from secondary cements. All
969 carbonate samples analyzed in this study were composed of > 70% primary carbonate grains or
970 micrite and < 30% post depositional diagenetic cements (estimated visually in hand sample and
971 thin section) except when secondary veins were specifically targeted for analysis. To create the
972 records of environment-specific deposits, a composite stratigraphic column of the MD and KD
973 sections was created (Fig. 5F). Intertidal deposits included tepees and oncolites, which in the
974 Khufai Formation are associated with the shallowest tufted and irregular laminites and tepees.

975 Storm deposits included edgewise conglomerates, intraclast conglomerates, ooid grainstones,
976 and hummocky cross stratification. Silt deposits included silt and cover, which we assume to
977 primarily be silt in the Shuram and Buah formations in the Huqf.

978 **Bulk powder x-ray diffraction (XRD)** XRD measurements were made on each powder used
979 for clumped isotope measurements on a PANalytical X'Pert Pro within the Material Science
980 at the California Institute of Technology. Scans were run from 5–70° 2θ with a step size of
981 0.008 and a scan step time of 10.16 s. A Cu anode was used at 45 kV and 40 mA. A zero-
982 background silicon plate was used for all measurements because of our small sample sizes.
983 Mineralogical phases were initially identified using the X'Pert Highscore IDMin function in
984 Jade. To determine relative abundances of calcite and dolomite in each sample, the relative peak
985 height intensities of the major calcite and dolomite peaks at 29.5° 2θ and 30.7° 2θ, respectively,
986 were used(23). Mixtures of known compositions of 100%, 80%, 60%, 40%, 20% and 0% calcite
987 with dolomite were used to create the following relationship of peak height to % dolomite for
988 the PANalytical X'Pert Pro setup at Caltech:

$$\%Dolomite = \frac{\frac{R.I.CaMg(CO_3)_2}{R.I.CaMg(CO_3)_2 + CaCO_3} - 0.0526}{0.0099}$$

989 90% of the samples analyzed were pure end-members of either calcite or dolomite. For the 10%
990 of samples that were a mixture of both calcite and dolomite, the acid digestion fractionation for
991 δ¹⁸O and min-water fractionation factor for all mixtures in the clumped isotope calculations
992 were made assuming 100% composition of the dominant mineralogy. This will introduce a
993 systematic bias for values reported from those samples, but very few samples have subequal
994 (<70:30) carbonate mineral abundances.

995 **SEM/electron microprobe** A ZEISS 1550 VP Field Emission Scanning Electron Microscope
996 (SEM) equipped with an Oxford INCA Energy 300 x-ray Energy Dispersive Spectrometer

997 (EDS) system within the California Institute of Technology Geological and Planetary Sciences
998 Division Analytical Facility was used for high-resolution imaging of each sample. Images were
999 collected at a working distance between 7-9 mm using a Quadrant Back Scattering Detector
1000 (QBSD). In addition EDS spectroscopy measurements of individual minerals were made to
1001 identify the types of detrital minerals present in a given sample. Electron Backscatter Diffraction
1002 (EBSD) analyses were performed using Oxford AZtecHKL acquisition software on sam-
1003 ples with 2.5-5 μm carbon coats. Kikuchi bands were collected using 20kV accelerating voltage
1004 at 70° tilt with step sizes between 0.4 and 1 μm . Data were analyzed using Oxford HKL Channel
1005 5 software to map grain boundaries and preferred orientation.

1006 Cryo-fracturing experiments were conducted on dolomitic oolites from Khufai Dome and
1007 Wadi Shuram. Samples were submerged in liquid nitrogen and then broken on removal. The
1008 broken face was gold coated and imaged on a Phenom XL SEM at MIT.

1009 Quantitative elemental spot analysis and elemental mapping on the various carbonate com-
1010 ponents to assess trace metal variability between textures was conducted on the JEOL JXA-8200
1011 Electron Microprobe. For all quantitative results, the accelerating voltage was 15 kV, the beam
1012 current was 20 nA, and the beam size was 1 μm . The CITZAF method was used for matrix
1013 correction. Sample standards for the five chemical elements analyzed, included: calcite for Ca,
1014 dolomite for Mg, siderite for Fe, rhodochrosite for Mn, strontianite for Sr, and anhydrite for
1015 S. Ca had an average detection limit of 177 ppm, Mg–283 ppm, Fe–323 ppm, Mn–300 ppm,
1016 Sr–589 ppm, and S–104 ppm.

1017 **Bulk powder inductively coupled plasma optical emission spectroscopy (ICP-OES)** Bulk
1018 ICP measurements were completed at Actlabs and at the Jet Propulsion Laboratory (JPL) on
1019 splits of the same drilled powder. The Actlabs method digested up to 0.5 g of sample with aqua
1020 regia (HCl + NO₃) for 2 hours at 95°C. Partial reactions are possible for some silicates with

1021 this dissolution method. Samples were then analyzed using a Varian ICP-OES for 35 elements.
1022 To target only the bulk limestone between 10 and 80 mg of material was digested in 10% acetic
1023 acid for 24 hours at 25°C at the California Institute of Technology. Samples were then filtered
1024 to remove particulate oxides and diluted with HCl to minimize introduction issues with the Ar
1025 plasma source. Samples were analyzed at the Jet Propulsion Laboratory using a Thermo iCAP
1026 6300 radial view ICP-OES with a Cetac ASX 260 autosampler with solutions aspirated to the
1027 Ar plasma using a peristaltic pump. Three standard solutions of 0.5 ppm, 5 ppm and 50 ppm of
1028 Mn, Al, Ca, K, Mg, S, Fe and Na, and three standard solutions of 0.1 ppm, 1 ppm and 10 ppm
1029 Sr in an acetic-HCl solution to matrix match were run between every 8 sample unknowns.

1030 **Bulk powder x-ray absorption near edge spectroscopy** X-ray absorption near-edge spec-
1031 troscopy (XANES) was conducted at the Stanford Synchrotron Radiation Lightsource (SSRL)
1032 on beam line 4-1 on five representative bulk powdered samples from the Shuram Formation in
1033 Central Oman. Samples were collected using a 3 mm rotary drill bit and further powdered using
1034 a mortar and pestle. The powdered samples were spread in a monolayer over Scotch tape and
1035 then covered with a second layer of Scotch tape. Approximately 8–16 Scotch tape layers were
1036 used for each sample, to maximize both absorbance and transmission. We used a silicon 220 $\Phi=$
1037 90 crystal and x-ray absorption spectra (XAS) were collected on a Ge multi-element detector for
1038 fluorescence and on an absorption detector for transmission spectra. A collimating mirror was
1039 used to reduce beam harmonics. XANES spectra of both Fe and Mn spectra were generated for
1040 each sample with a scan from 6310–7502 eV. Samples were then normalized for each element
1041 and compared to XANES spectra of known standards analyzed under similar conditions.

1042 **Secondary ion mass spectrometry (SIMS)** In situ analysis of $\delta^{13}\text{C}_{VPDB}$ and $\delta^{18}\text{O}_{VPDB}$ was
1043 conducted using SIMS analysis on a Cameca 7f-GEO in the Center for Microanalysis at the
1044 California Institute of Technology. The Cameca 7f-GEO was run at a mass resolving power for

1045 C of 3000 and for O of 1800. Two thick sections of samples from the nadir of the excursion
1046 from the Mukhaibah Dome (MD) and Khufai Dome (KD) sections were embedded with in-
1047 house carbonate standards prior to polishing (Fig. S9). A 10 kV Cs⁺ beam was held at 0.4 nA
1048 for C analyses and 1.1 nA for O analyses for spot sizes of 30 μm and 40 μm, respectively. Each
1049 spot was pre-sputtered for 120 s. Oxygen was measured on a two Faraday cups for a count
1050 time of 0.96 s for ¹⁶O and 4.96 s for ¹⁸O using a fast mass peak switching system. Carbon was
1051 measured on a single EM with a count time of 0.96 s for ¹²C and 10.0 s for ¹³C. Secondary ions
1052 were collected at 9 kV. 10 measurements of sample unknowns were bracketed with 4 standard
1053 analyses. Standard deviation was better than 1‰ for δ¹³C and δ¹⁸O for each of the 8 standard
1054 analyses bracketing sets of unknowns.

1055 **Carbonate clumped isotope thermometry** All samples plotted were previously published
1056 in (16). Refer to that reference for methods, data processing, analysis and petrographic and
1057 hand sample context.

1058 **Carbonate carbon and oxygen isotopic analysis** In addition to the clumped isotope mea-
1059 surements described above, new high resolution δ¹³C and δ¹⁸O data across the Shuram and
1060 Buah formations was analyzed at the California Institute of Technology on a ThermoFinnigan
1061 Delta V Plus attached to a ThermoFinnigan GasBench II. This data was combined with isotopic
1062 data from the Khufai Formation (39). For the samples analyzed at Caltech, approximately 300
1063 μg of carbonate were weighed into gas vials, flushed with UHP He for 5 minutes and reacted
1064 with 100% H₃PO₄ at 78°C for 1 hour within the ThermoFinnigan GasBench II. Three standards
1065 were run at the beginning of an 88 sample run and then 8 unknown samples were bracketed by
1066 1 standard. Standard reproducibility was better than 0.2‰ in δ¹³C and better than 0.35‰ and
1067 0.5‰ for δ¹⁸O for two in-house standards. Additional samples were analyzed at the University
1068 of California, Riverside and University of Nevada, Las Vegas using a similar ThermoFinnigan

1069 GasBench setup. Samples analyzed at the University of Michigan weighing a minimum of 10
1070 μg were placed in stainless steel boats. Samples were roasted at 200°C in vacuo for one hour
1071 to remove volatile contaminants and water. Samples were then placed in individual borosili-
1072 cate reaction vessels and reacted at $77^\circ \pm 1^\circ\text{C}$ with 4 drops of anhydrous phosphoric acid for 8
1073 minutes for calcite (12 minutes for dolomites) in a ThermoFinnigan MAT Kiel IV preparation
1074 device coupled directly to the inlet of a ThermoFinnigan MAT 253 triple collector IRMS. ^{17}O
1075 corrected data are corrected for acid fractionation and source mixing by calibration to a best-fit
1076 regression line defined by two NBS standards, NBS18 and NBS19. Data are reported in delta
1077 notation relative to VPDB. Precision and accuracy of data are monitored through daily analysis
1078 of a variety of powdered carbonate standards. At least four standards are reacted and analyzed
1079 daily. Measured precision is maintained at better than 0.1‰ for both carbon and oxygen isotope
1080 compositions.

1081 **Isotopic and Elemental Compilation** A literature search was conducted to locate published
1082 carbonate isotopic and trace element data (i.e. Mn, Sr, etc.) and $\delta^{13}\text{C}_{org}$ from platform carbon-
1083 ates for Fig. 5. The $\delta^{18}\text{O}$ data from these individual studies of bulk rock $\delta^{13}\text{C}$ had not been
1084 previously compiled in a systematic way with a high-resolution age model. Study level isotopic
1085 datasets from the literature were digitized into .csv files, and metadata were added (location,
1086 mineralogy, type of material, Formation name, etc.). We calculated temperature using a water
1087 $\delta^{18}\text{O}_{VSMOW}$ value of -1.2‰ . We used mineral-specific fractionation factors for calcite sam-
1088 ples (84) and dolomite samples (85). $\delta^{13}\text{C}_{org}$ data are divided into inner shelf environments (9),
1089 outer shelf environments (70, 86, 87), and basinal environments (71). Ages of Gaskiers are
1090 from (88).

1091 **Data included in isotopic and elemental compilation :**

1092 Ediacaran: (39, 70, 71, 74, 86, 87, 89–96)

1093 $^{87}\text{Sr}/^{86}\text{Sr}$: (66)

1094 **Age Model** We created a consistent age model for all individual studies and opted not to use
1095 previously published age models individual authors may have created. Age models were built
1096 using information provided within the datasets, stratigraphic columns, and text of compiled
1097 articles. For all points in the dataset, ages were interpolated using a linear model assuming
1098 a constant sedimentation rate between tie points. Sedimentation rates were error checked for
1099 consistency. The age model for compiled $\delta^{18}\text{O}$ Proterozoic datasets utilized U/Pb and Re/Os
1100 ages from the published literature (69, 74) and $\delta^{13}\text{C}$ excursions were used to build a new age
1101 model for each study, except (66, 74).

1102 **Volcanism Compilation** A literature search was conducted to locate published dates of Neo-
1103 proterozoic igneous activity including both extrusive and intrusive deposits. Information in-
1104 cludes name, location, size estimates if they exist, type of deposit, age and error on the age.

1105 **Data included in volcanism compilation** :

1106 (51, 97–128)

1107

1108 **Per Capita Extinction and Origination Rates** We first calculated FAD and LAD from oc-
1109 currences we tabulated for Neoproterozoic microfossils from (73, 76, 77) and Neoproterozoic
1110 Ediacaran fauna from (129), separated into deep water and shallow water occurrences. We cal-
1111 culate per capita extinction and origination rates (130) on these three compilations using 3 Myr
1112 bins without subsampling. The age constraints we used for fossil occurrences in the Neopro-
1113 terozoic are included in a Supplemental Table and in the OSF repository. Results are normalized
1114 to the largest per capita extinction or origination rate in each of the four records.

1115 **2 Supplementary information**

1116 **Geologic Setting** In central Oman, the Khufai Formation is composed of shallow-water car-
1117 bonates deposited on a carbonate ramp. The carbonates in the Huqf show a generalized up-
1118 ward shallowing of the lithofacies and lateral progradation. The lower Khufai Formation is
1119 composed of medium to thick intraclast wackestone event beds deposited below storm weather
1120 wave base (20). In contrast, the middle and upper Khufai Formation was deposited in a peritidal
1121 environment with minimal accommodation space, and restriction and evaporation. These rocks
1122 display petrographic evidence for an early, fabric-retentive, dolomite formation process (20, 44).
1123 Lithofacies include cross-bedded oncolite grainstone, tufted laminite, domal stromatolites, intr-
1124 aclast conglomerate and structures including teepees associated with evaporite mineral pseudo-
1125 morphs and brecciation (Fig. 1, Fig. S1) (20). The most proximal facies in the Upper Khufai
1126 Formation (i.e., teepees and breccia) are overlain by aggrading stromatolites and oolitic grain-
1127 stone marking a sequence boundary exists where the depositional environment changes from
1128 one dominated by exposure to one characterized by slow flooding and increased accommoda-
1129 tion space (20). The carbonate strata above the sequence boundary preserve the initial decline
1130 in $\delta^{13}\text{C}$ and $\delta^{18}\text{O}$ values of the Shuram excursion. The dolomitic lithofacies of the uppermost
1131 Khufai, including stromatolites and cross-stratified ooid grainstone record $\delta^{13}\text{C}_{VPDB}$ values as
1132 low as -8.5‰ (Fig. 1, Fig. S1). One would predict this transition from a restricted evapo-
1133 rative environment to a flooded platform in closer connection with open marine water would
1134 be accompanied by an isotopic change in the fluid oxygen isotope composition. The maximal
1135 transgression and flooding is coincident with the introduction of massive, poorly bedded red
1136 siltstone deposits and a general loss of carbonate lithofacies marking the start of the siliciclastic
1137 dominated Shuram Formation (Fig. 1) (20, 41). The middle and upper Shuram Formation is
1138 better exposed in outcrop and consists of repeated parasequences of hummocky cross-stratified

1139 siltstone capped by trough to planar cross-stratified limestone ooid grainstone with $\delta^{13}\text{C}_{VPDB}$
1140 values as low as -12‰ (Fig. 1, Fig. S1) (23, 41). The siltstone contains abundant evidence for
1141 soft sediment deformation including ball and pillow structures (23). The recovery of the Shu-
1142 ram excursion occurs in the lower Buah Formation, which is also composed of shallow-water
1143 carbonates that indicate a general upward shallowing of the lithofacies. The lowermost Buah
1144 is composed of limestone crinkly laminite and edgewise conglomerate, a lithofacies interpreted
1145 as a partially lithified seafloor that is reworked and stacked on edge by oscillatory wave action
1146 (Fig. 1, Fig. S1) (131). This reworking of the seafloor likely occurred during storm events.
1147 The gradual isotopic recovery continues above a sequence boundary that shows a rapid increase
1148 in accommodation space, a shutoff in the siliciclastic input and the aggradation of large reefal
1149 stromatolite mounds filled in with trough cross-stratified grainstone shoals (Fig. S1).

1150 In the Oman Mountains the Khufai Formation is thinner, completely limestone and is pre-
1151 dominantly intraclast wackestone and mudstone deposited as turbidites below storm weather
1152 wave base. The Upper Khufai Formation is marked by successive large-scale (3 m) slump
1153 beds and in a few locations including Wadi Bani Awf significant coarse grained sandstone
1154 beds (20, 41). The Shuram Formation is dominantly composed of siltstones alternating with
1155 ripple-stratified silty carbonate grainstone beds with gutter casts on bed bottoms. The ripples
1156 indicate significant aggradation during ripple formation producing asymmetrical climbing wave
1157 ripple morphologies (Fig. 1, Fig. S1) (41). The Buah Formation has a broadly similar lithofa-
1158 cies progression to the Huqf outcrop area with more significant lithofacies differences between
1159 Wadi Hajir and Wadi Bani Awf, the latter being more distal (43, 132).

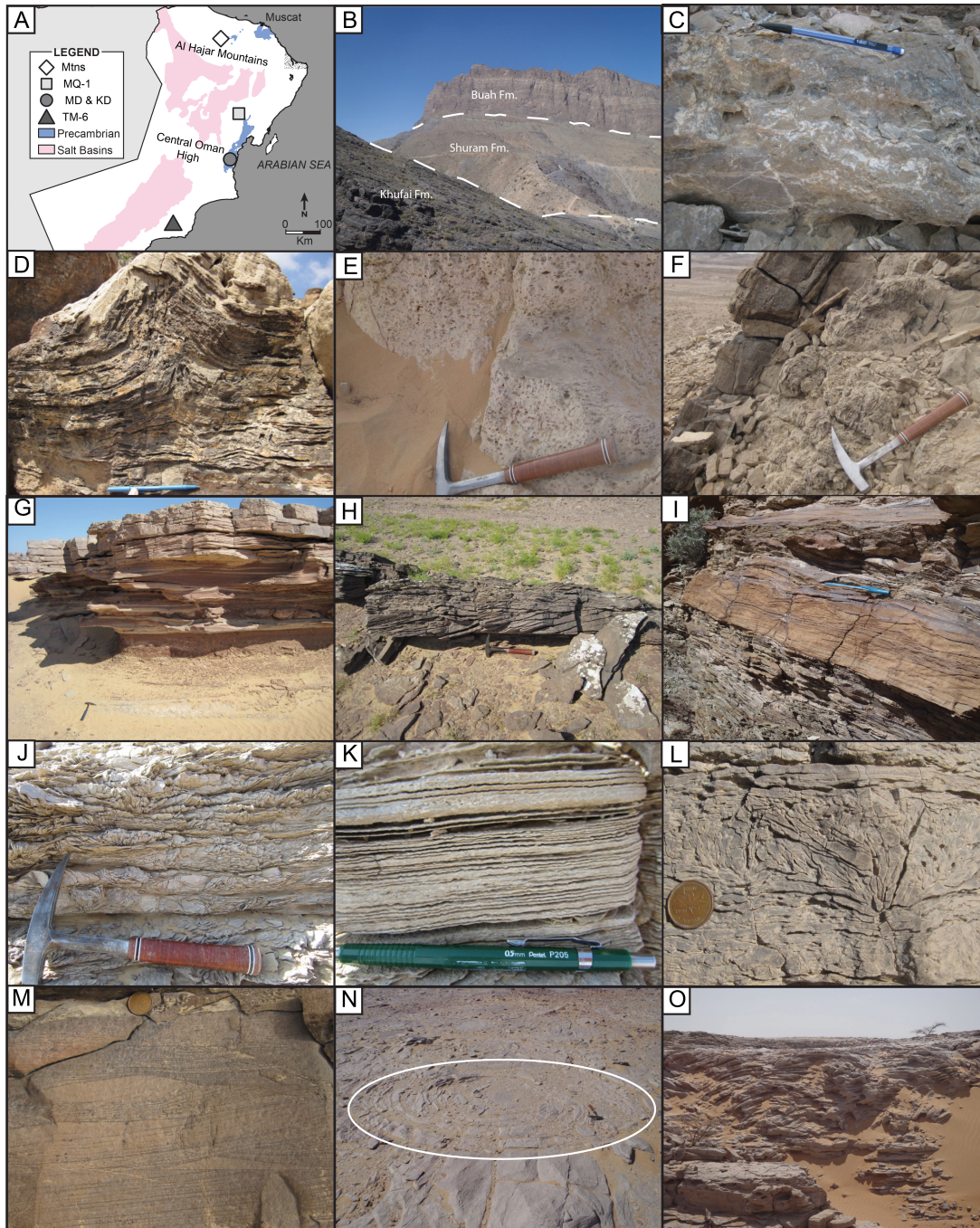
1160 **Considerations for interpreting the Δ_{47} results** Here we discuss potential effects of burial
1161 history, diffusive solid state reordering, and mixing on the interpretation of the clumped isotope
1162 signal across the Shuram excursion. Relevant discussion can also be found in (16). Maximum

1163 burial depth of the Huqf-Haushi Outcrop Area can be estimated a variety of ways. The Huqf-
1164 Haushi Outcrop Area is interpreted as an area dominated by long term uplift surrounded by
1165 the down faulted Masirah Trough and the subsiding Ghaba Salt Basin (133, 134). The Huqf
1166 Supergroup in the Huqf-Haushi Outcrop Area has large-scale folds trending WSW-ENE to
1167 NNE-SSW (133). These folds result in the Khufai Formation preserved in outcrop as a se-
1168 ries of steeply dipping (45° or less) anticlines surrounded by shallowing dipping Shuram and
1169 Buah Formation synclines. The gently dipping to flat lying Ordovician Mahatta Humaid For-
1170 mation and Upper Carboniferous/Lower Permian Haushi Group onlap the outcrops of the Huqf
1171 Supergroup. Both the Ordovician and late Paleozoic deposits display no structural folding sug-
1172 gesting the deformation and uplift occurred during or shortly after deposition of the Huqf Su-
1173 pergroup (133, 135). Clay mineralogies within the Shuram and Buah Formations include illite,
1174 illite-smectite complexes, smectite and kaolinite (136) which suggests the Huqf-Huashi Out-
1175 crop Area hasn't experienced the full smectite-to-illite transition (burial <3000 m). Based on
1176 the structural history of the Huqf-Haushi Outcrop Area, we interpret the KD and MD sec-
1177 tions as the shallowest buried of all samples analyzed for clumped isotope thermometry from
1178 Oman (16). As a whole the organic material from the Neoproterozoic Huqf Supergroup across
1179 Southern and Central Oman preserves a range of molecular biomarkers and sits in the marginal
1180 to middle oil window, representing some of the least thermally altered sediments of this time
1181 interval (137, 138).

1182 The importance of diffusive solid state reordering on the clumped isotope thermometer has
1183 been estimated using laboratory heating experiments and reaction models (139–141). Esti-
1184 mates for optical calcite and brachiopod calcite indicate 1% reordering would occur between
1185 115 - 127°C if the sample were held at those temperatures for 10 Ma and 101 - 112°C for 100
1186 Ma. To achieve 99% reordered calcite in 10 Ma the modeled temperature range is 163 - 174°C
1187 or 144 - 155°C in 100 Ma (141). Evidence from blocking temperatures derived from marbles

1188 indicates dolomite will be much less susceptible to solid state reordering (*139, 142*). Dolomite
1189 marbles yield blocking temperatures of $\sim 300^{\circ}\text{C}$ whereas calcite marbles yield temperatures
1190 ranging from $150\text{-}200^{\circ}\text{C}$ (*139, 143*). If a stratigraphic section reached temperatures able to
1191 drive diffusive reordering in calcite but not dolomite, we expect the calcitic samples to yield
1192 consistently higher temperatures and calculated ^{18}O -rich compositions for the fluid. Instead,
1193 calcitic samples from the recovery in the upper Shuram Formation yield similar temperatures to
1194 the pre-excursion upper Khufai Formation. Samples from the uppermost dolomites of the Khu-
1195 fai Formation yield similar temperatures and fluid oxygen isotope compositions to calcites from
1196 the lower and middle Shuram Formation. The combined estimates for minimal burial history
1197 from organic preservation and mineralogical similarities between calcite and dolomite suggest
1198 diffusive solid state reordering is not a significant process in these rocks (*16*).

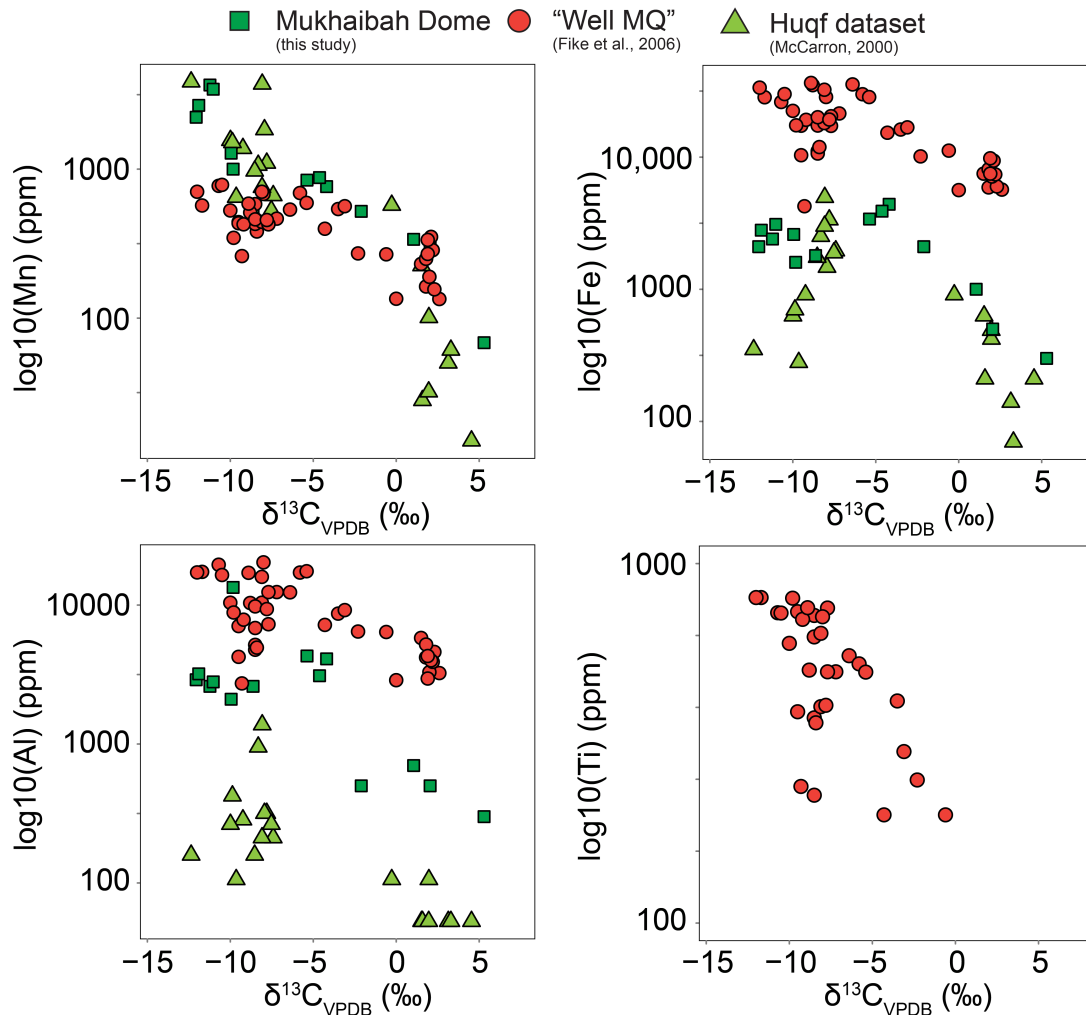
1199 Apatite thermochronology has similar to lower temperature sensitivities as calcite clumped
1200 isotope solid state re-ordering does for 100 Ma timescales and provides another point of com-
1201 parison for maximum burial temperatures. Fission track ages from Huqf Supergroup detrital
1202 apatites, sourced from the 650-750 Ma granitic basement, range from 600 - 400 Ma with a peak
1203 at 450 Ma in wells from eastern Oman (*144*). This data suggests some wells never reached
1204 the apatite closure temperature of $\sim 100^{\circ}\text{C}$ during burial and other wells experienced signifi-
1205 cant uplift around 450 Ma and saw maximum temperatures $< 100^{\circ}\text{C}$ for the remainder of the
1206 Phanerozoic. Samples buried more deeply in the western part of Oman give more recent fission
1207 track ages indicating partial annealing (*144*).



1208

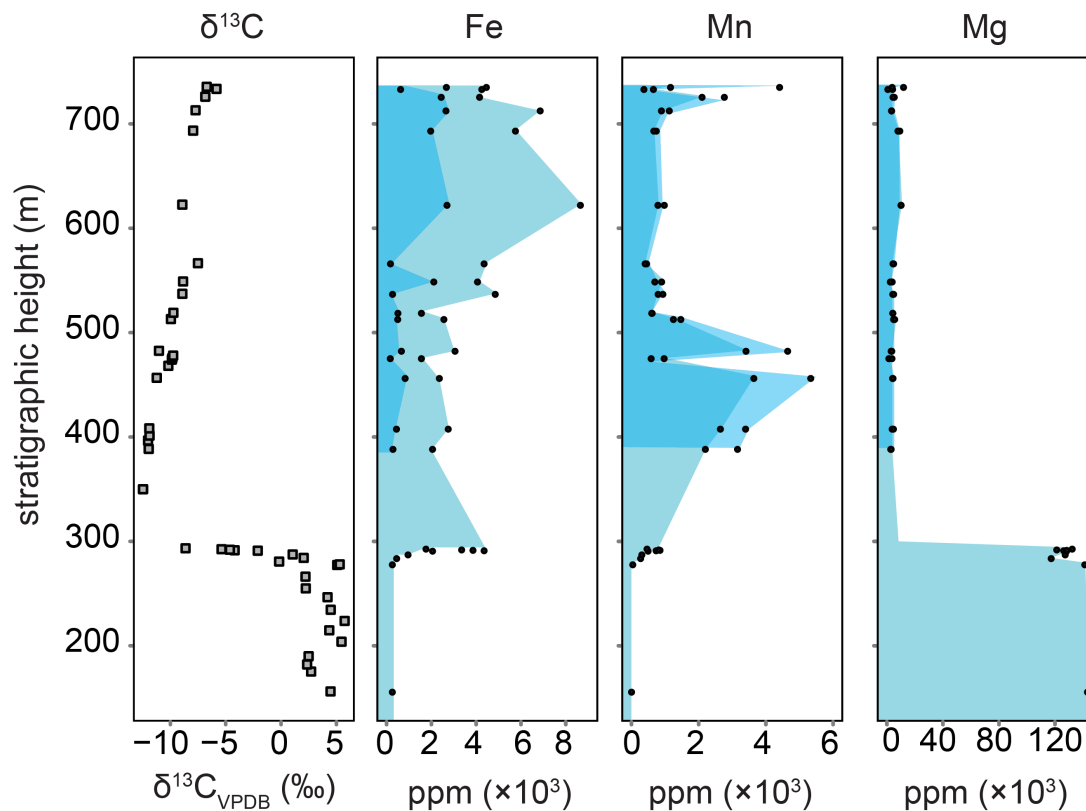
1209 **Fig. S1. Geologic context of the Shuram excursion.** (a) Location map of the five stratigraphic
 1210 sections analyzed. (b) Mountainside views of the three formations capturing the excursion in
 1211 the Oman Mountains. (c) Diagenetic calcite from the Lower Khufai Formation. (d, e) Periti-

1212 dal tepee and fenestral mudstone from the Upper Khufai Formation. **(f)** Transgressive systems
1213 tract recording the onset of the negative excursion in the Upper Khufai Formation. **(g, h)** Hum-
1214 mocky cross-stratified siltstones capped by ooid grainstones in the middle Shuram Formation.
1215 **(i)** Climbing ripples in the Shuram Formation from the Oman Mountains. **(j, k, l)**, Edgewise
1216 conglomerate and crinkly laminite from the lower Buah Formation. **(m, n, o)** intraclast con-
1217 glomerate and stromatolites bioherms from the Buah Formation.



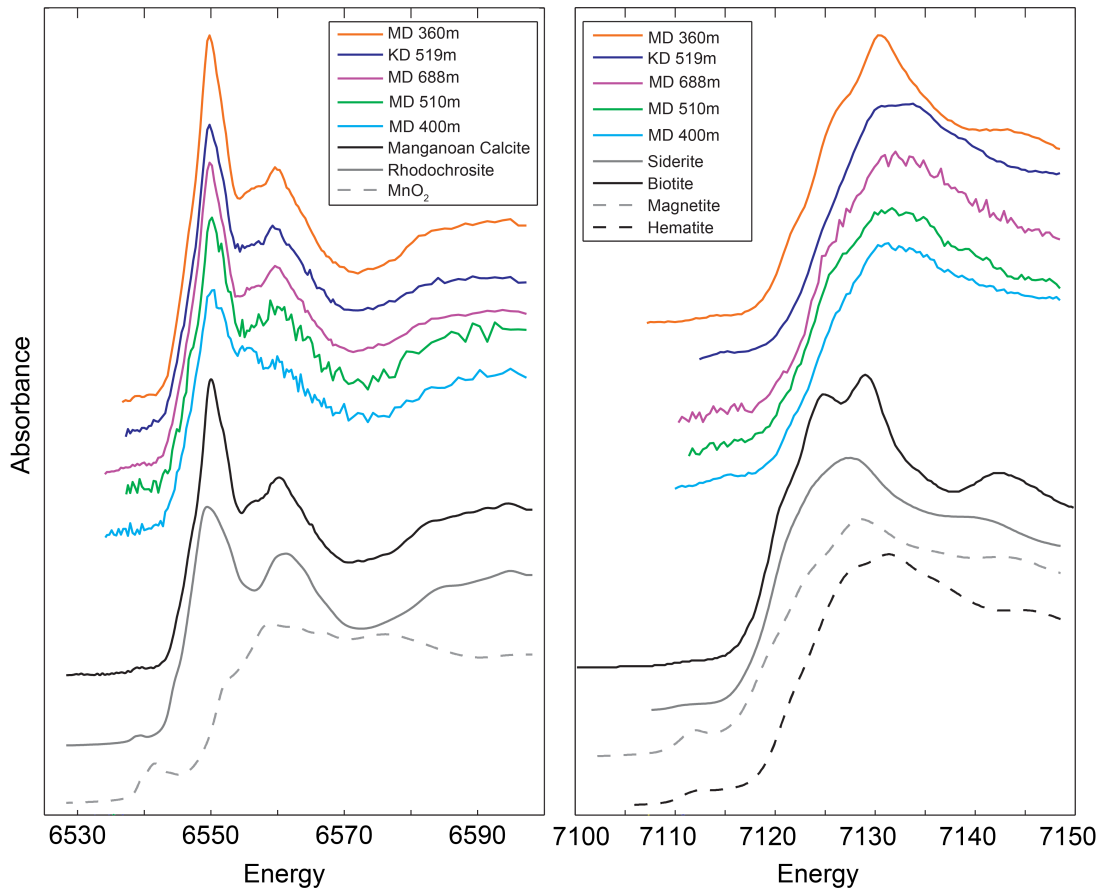
1218

1219 **Fig. S2. Cross plots of bulk trace metal measurements versus $\delta^{13}\text{C}$.** a Log(Fe), log(Mn),
 1220 log(Ti) and log(Al) versus $\delta^{13}\text{C}$ from three of the different sections analyzed. The magnitude of
 1221 Fe, Al and Ti is higher for Well 'MQ' because that study dissolved well cuttings containing both
 1222 siliciclastic and carbonate components in a strong acid as opposed to preferentially sampling
 1223 carbonate. Data from this study and (9, 145).



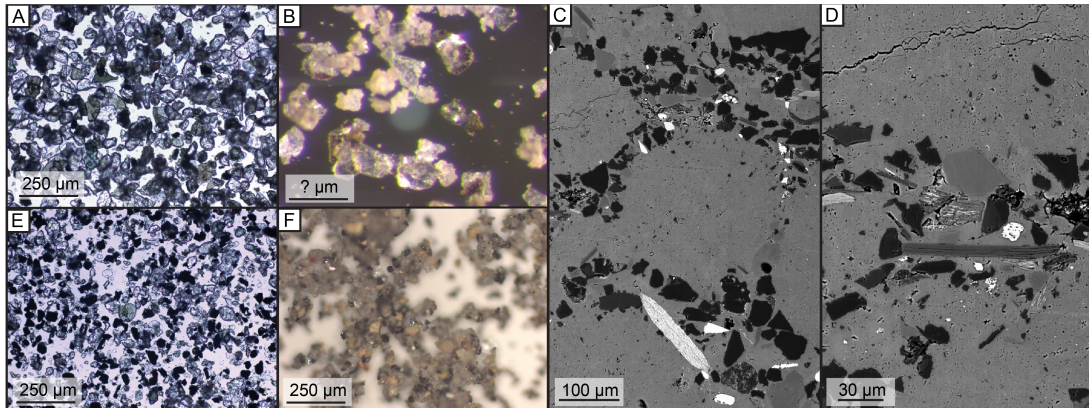
1224

1225 **Fig. S3. Bulk strong acid (aqua regia) and acetic acid trace metal measurements from**
 1226 **section MD for Fe, Mn and Mg.** A strong acid dissolution (light blue) vs. an acetic acid
 1227 dissolution (dark blue) targeting only the limestone indicates a significant component of the iron
 1228 signal is not carried in the carbonate while most of the manganese signal is. The magnesium
 1229 concentration confirms the observed mineralogical change to limestone.



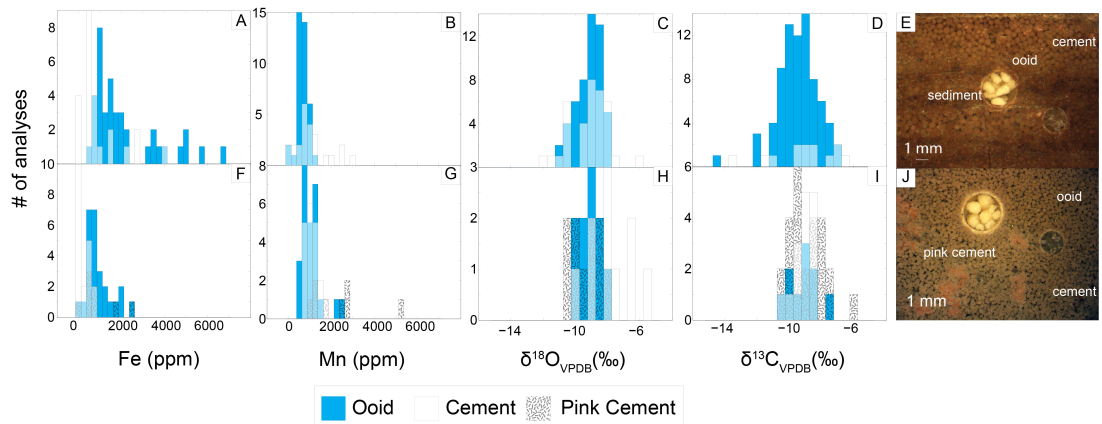
1230

1231 **Fig. S4. Bulk XANES spectra of samples from the Shuram Formation.** XANES spectra
 1232 of samples from the nadir of the excursion yield consistent results indicating the iron is found
 1233 in two phases hematite and biotite while the manganese is present as Mn(II) and most closely
 1234 matches the spectra of manganooan calcite.



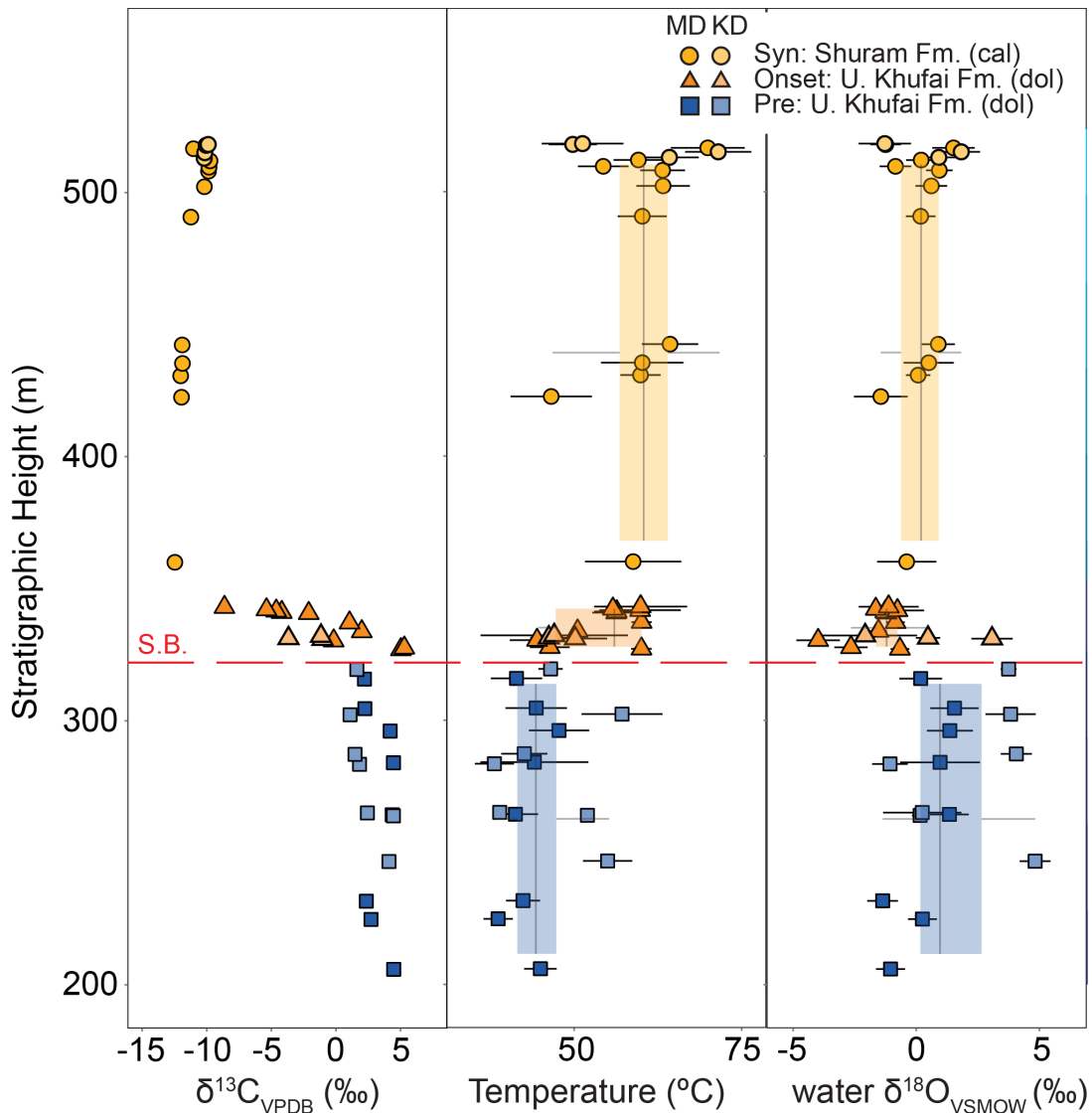
1235

1236 **Fig. S5. Siliciclastic fraction of the Shuram (a–d) and Johnnie formations (e–f).** (a, e) Wet
 1237 grain mount under 10X magnification with visible biotite and muscovite grains. Iron oxides are
 1238 more abundant in the sample from the Johnnie Formation. (b, f) Dry grain mount with quartz,
 1239 muscovite, biotite, iron oxides and feldspars visible. The coarser grains from a fine-grained
 1240 sandstone from the Shuram Formation include poorly weathered micas. (c, d) SEM images of
 1241 iron-rich biotite grains within the detrital sediments filling in around the ooids.



1242

1243 **Fig. S6. Histograms of in situ geochemical data for two samples from the Shuram Forma-**
 1244 **tion. a, f** Spot analyses of iron (ppm) on ooids and two cement types—clear blocky cements
 1245 and pink microcrystalline cements. **b, g** Spot analyses of manganese (ppm). **c, h** Spot analyses
 1246 of $\delta^{13}\text{C}_{\text{VPDB}}$. **d, i**, spot analyses of $\delta^{18}\text{O}_{\text{VPDB}}$. **e, j** Images of each sample showing ooids, two
 1247 types of cements and embedded standards ($\pm 1\text{‰}$ SD).



1248

1249 **Fig. S7. Temperature and fluid oxygen isotope composition across the onset and nadir**

1250 **of the Shuram excursion.** (A) Detailed stratigraphic section of the onset of the $\delta^{13}\text{C}_{VPDB}$

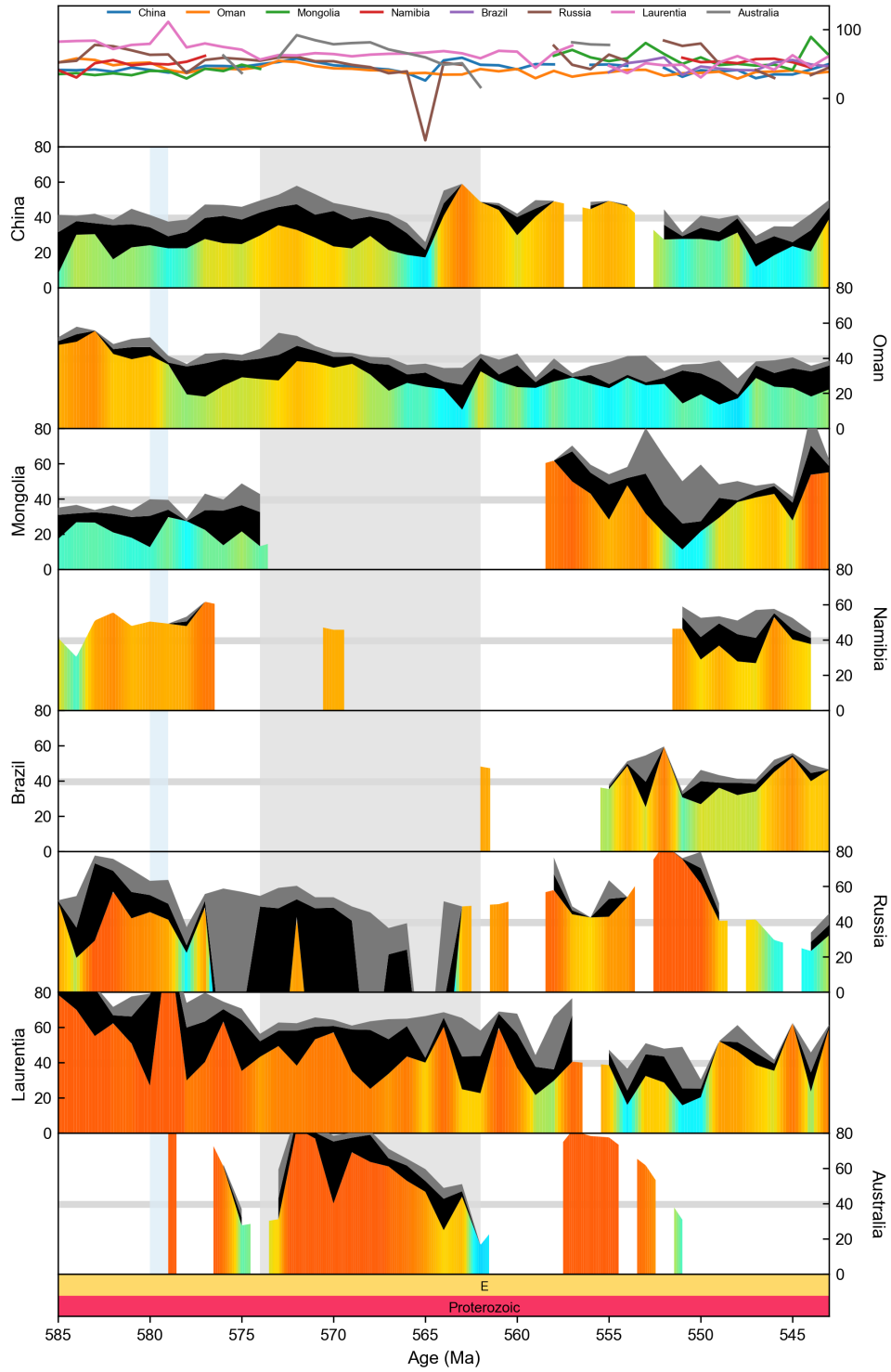
1251 excursion with corresponding temperature and water $\delta^{18}\text{O}_{VSMOW}$ for MD and KD sections.

1252 Boxplots showing the minimum, maximum, standard deviation and mean for each population –

1253 pre-excursion, onset, and syn-excursion are also shown. The temperature change estimate from

1254 the modes of the density distributions of pre-excursion to syn-excursion populations are listed.

1255 Circles are calcite.

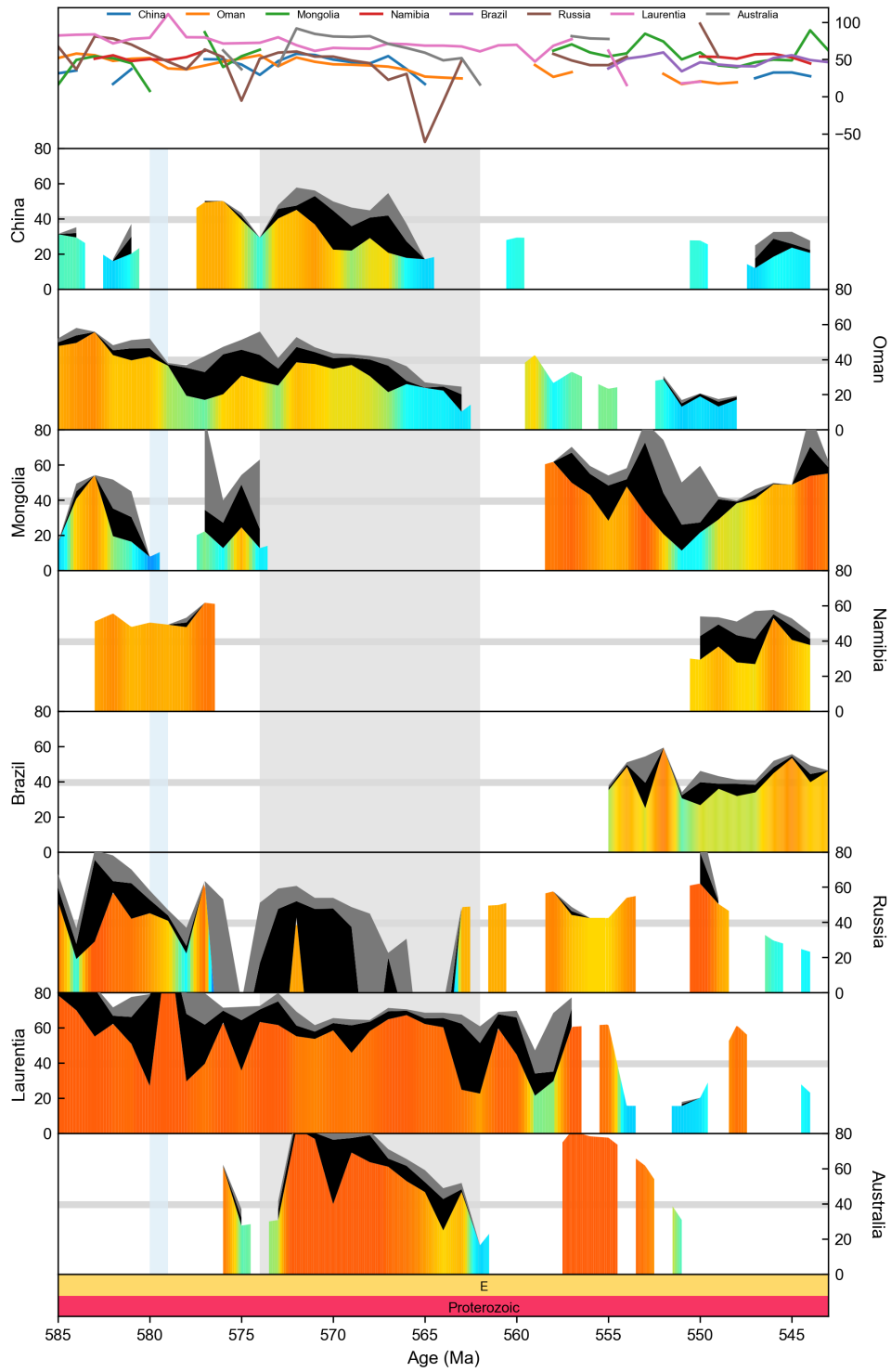


1256

1257 **Fig. S8. Ediacaran country-level contributions to the composite temperature record pre-**

1258 **sented in Fig. 5H.** (A) Temperature comparison of the different countries. (B-K) The 1st to
1259 25th quantiles (black) and 25th to 50th quantiles (grey) of shallow marine temperatures from
1260 Scenario 1 estimated using quantile regression on points within 1 Myr windows sampled each
1261 1 Myr. In panel order, data are plotted from China, Oman, Mongolia, Namibia, Brazil, Russia,
1262 Laurentia (USA and Canada), and Australia. Grey bands represent the upper temperature limit
1263 of modern tropical subtidal ectotherms (146). Vertical bars indicate the Gaskiers glaciation
1264 (light blue) and the Shuram excursion (grey)

1265



1266

1267 **Fig. S9. Ediacaran country-level contributions from limestone only to the composite tem-**

1268 **perature record presented in Fig. 5H. (A)** Temperature comparison of the different countries.
1269 **(B-K)** The 1st to 25th quantiles (black) and 25th to 50th quantiles (grey) of shallow marine tem-
1270 peratures from Scenario 1 estimated using quantile regression on points within 1 Myr windows
1271 sampled each 1 Myr. In panel order, data are plotted from China, Oman, Mongolia, Namibia,
1272 Brazil, Russia, Laurentia (USA and Canada), and Australia. Grey bands represent the upper
1273 temperature limit of modern tropical subtidal ectotherms (*146*). Vertical bars indicate the Gask-
1274 iers glaciation (light blue) and the Shuram excursion (grey)

1275

1276 **Table. S1. Datasets from this manuscript** Data from GPS, clumped isotope thermometry,
1277 XRD, bulk strong and weak acid trace metal analyses, SIMS, Electron microprobe and carbon
1278 and oxygen analyses.